ELSEVIER

Contents lists available at ScienceDirect

# Chemical Geology

journal homepage: www.elsevier.com/locate/chemgeo





# Apatites for destruction: Reference apatites from Morocco and Brazil for U-Pb petrochronology and Nd and Sr isotope geochemistry

Francisco E. Apen <sup>a,\*</sup>, Corey J. Wall <sup>b</sup>, John M. Cottle <sup>a</sup>, Mark D. Schmitz <sup>b</sup>, Andrew R. C. Kylander-Clark <sup>a</sup>, Gareth G.E. Seward <sup>a</sup>

#### ARTICLE INFO

Editor: Catherine Chauvel

Keywords: Apatite U-Pb geochronology Sr-Nd isotopes Laser ablation TIMS

#### ABSTRACT

In situ apatite U-Pb petrochronology and Sr-Nd isotope geochemistry requires well-characterized and matrixmatched references materials (RMs), yet only a few suitable apatite RMs are currently available. To ameliorate this issue, we determined the U-Pb, Sm-Nd, and Sr isotopic and elemental compositions of a suite of prospective apatite RMs using isotope dilution (ID) TIMS and laser ablation (LA) ICP-MS. The two RMs, from Morocco (MRC-1) and Brazil (BRZ-1), are cm-sized and available in significant quantities. The U-Pb ID-TIMS data yield an isochron age of 153.3  $\pm$  0.2 Ma for MRC-1. This age is consistent with laser ablation split stream ICP-MS (LASS) analyses that produce an isochron age of 152.7  $\pm$  0.6 Ma. The weighted mean of ID-TIMS analyses for  $^{143}$ Nd/ $^{144}$ Nd analyses is  $0.512677 \pm 3$ , for  $^{147}$ Sm/ $^{144}$ Nd is  $0.10923 \pm 9$ , and for  $^{87}$ Sr/ $^{86}$ Sr is  $0.707691 \pm 2$ . The range and mean of TIMS Sm-Nd isotopic data are reproducible by LA-ICP-MS, but laser ablation Sr data are consistently offset towards more radiogenic values. For BRZ-1 apatite, ID-TIMS U-Pb analyses are dispersed, but a subset of the data yields a coherent age intercept of 2078  $\pm$  13 Ma. The vast majority of LASS spot transects across the apatite produce an isochron that define a younger age of 2038  $\pm$  14 Ma. We interpret this as incorporation of cryptic, younger altered domains within BRZ-1. Discordant U-Pb spot analyses are associated with chemically distinct cracks, likely a result of fluid infiltration. The weighted means of ID-TIMS analyses of BRZ-1 yield  $^{143}\text{Nd}/^{144}\text{Nd} = 0.510989 \pm 5$ ,  $^{147}\text{Sm}/^{144}\text{Nd} = 0.10152 \pm 8$ , and  $^{87}\text{Sr}/^{86}\text{Sr} = 0.709188 \pm 3$ . The distribution of Nd isotopic compositions of this RM measured by LA-MC-ICP-MS analyses are comparable to TIMS analyses. By contrast, 87Sr/86Sr measurements by LA-ICP-MS are inaccurate and exhibit large uncertainties, but this RM can be useful for empirically correcting in situ <sup>87</sup>Sr/<sup>86</sup>Sr measurements. The data indicate that MRC-1 apatite may serve well as a U-Pb, Sm-Nd, and Sr RM, whereas BRZ-1 apatite has the most potential as a Sm-Nd RM. These potential RMs provide new benchmarks for in situ apatite chemical analyses and inter-laboratory calibrations.

## 1. Introduction

Apatite is common accessory mineral in a variety of rock types—both terrestrial and extra-terrestrial (Piccoli and Candela, 2002; Spear and Pyle, 2002; McCubbin and Jones, 2015)—and can host substantial amounts of U, Th, Sr, Nd, and other incompatible elements, making it a useful geochronometer and isotope tracer of petrogenetic processes (Spear and Pyle, 2002; Prowatke and Klemme, 2006; McFarlane and McCulloch, 2007; Horstwood et al., 2008; Chew et al., 2011; Henrichs et al., 2018). Accordingly, apatite studies have diverse applications including, but not limited to: resolving thermal histories in the 400–600 °C temperature range with the U-Pb system (e.g., Krogstad and

Walker, 1994; Chamberlain and Bowring, 2001; Schoene and Bowring, 2006, 2007; Chew et al., 2011; Cochrane et al., 2014; Seymour et al., 2016; Ibanez-Mejia et al., 2018; Kirkland et al., 2018; Paul et al., 2019; Apen et al., 2020), tracking sediment provenance (e.g., Morton and Yaxley, 2007; Carrapa et al., 2009; Henderson et al., 2010; Chew et al., 2011; Thomson et al., 2012; Bruand et al., 2017; O'Sullivan et al., 2018, 2020; O'Sullivan and Chew, 2020), use as a pathfinder for mineral deposits (e.g., Belousova et al., 2002; Mao et al., 2016; Glorie et al., 2019), and fingerprinting the petrogenesis of metamorphic and igneous rocks with Sr or Nd isotopes, providing insights into the growth and modification of Earth's oldest continental fragments (e.g., Emo et al., 2018; Hammerli et al., 2019; Antoine et al., 2020; Bruand et al., 2020; Fisher

<sup>&</sup>lt;sup>a</sup> Department of Earth Science, University of California, Santa Barbara, CA 95136, USA

<sup>&</sup>lt;sup>b</sup> Department of Geosciences, Boise State University, Boise, ID 83706, USA

<sup>\*</sup> Corresponding author.

E-mail address: apen@ucsb.edu (F.E. Apen).

et al., 2020a, 2020b; Ravindran et al., 2020; Gillespie et al., 2021b). Coupled with the relatively rapid acquisition and high-spatial resolution capabilities of in situ microbeam methods—laser ablation inductively coupled plasma mass spectrometry (LA-ICP-MS) and secondary-ion mass spectrometry (SIMS) (e.g., Sano et al., 1999; Chew et al., 2011, 2017; Kylander-Clark, 2017; Gillespie et al., 2021a)—geochronological and geochemical analyses of apatite are increasingly commonplace. Despite the rising use of apatite petrochronology and geochemistry, suitable apatite reference materials (RMs) available for inter-laboratory comparisons (homogeneous, well-characterized, and accessible) are scarce.

A critical component of in situ isotopic and elemental analyses by LA-ICP-MS is monitoring and correcting for plasma- and laser-induced element fractionation (Horn et al., 2000; Sylvester, 2008; Paton et al., 2011; Fisher et al., 2020b). As the degree of fractionation is related to the physical structure and chemical composition of the ablated material, robust corrections necessitate matrix-matched and isotopically-homogeneous RMs (e.g., Chew et al., 2014a). Among the

**Table 1**U-Pb age summary of some apatite RMs.

Apatite	Origin	Reported age (Ma) <sup>a</sup>	Method <sup>b</sup>	References
Durango	Durango, Mexico	$31.4 \pm 0.2$	Ar-Ar (feldspar)	McDowell et al. (2005)
Durango		$32.7\pm0.1$	U-Pb ID- TIMS	Paul et al. (2021)
Emerald Lake	British Columbia, Canada	$92.2\pm0.9$	U-Pb ID- TIMS (titanite)	Coulson et al. (2002)
		$90.5\pm3.1$	U-Pb LA- SC-ICP-MS	Chew et al. (2011)
Kovdor	Kola Peninsula, Russia	$380.6 \pm \\2.6$	U-Pb ID- TIMS	Amelin and Zaitsev (2002)
MAD1	Madagascar, Africa	486.6 ± 0.9	U-Pb ID- TIMS	Thomson et al. (2012)
MAD2		474.3 ± 0.4	U-Pb ID- TIMS	Thomson et al. (2012)
MAD2-TCD		475.4 ± 1.8	U-Pb ID- TIMS	Fisher et al. (2020b)
	Colorado, United States	$523.5 \pm \\ 1.5 \\ 524.6 \pm$	U-Pb ID- TIMS U-Pb ID-	Schoene and Bowring (2006) Krestianinov et al.
McClure		$\begin{array}{c} 2.7 \\ 523.5 \pm \\ 1.7 \end{array}$	TIMS U-Pb ID- TIMS	(2021) Schoene and Bowring (2006) with Krestianinov et al. (2021)
401	Iran	$530.3 \pm \\1.5$	U-Pb ID- MC-ICP- MS	Thompson et al. (2016)
401		$506.2 \pm \\7.0$	U-Pb LA- MC-ICP- MS	Thompson et al. (2016)
Cheever mine	New York, United States	$907\pm14$	U-Pb ID- TIMS	Krestianinov et al. (2021)
Old Bed mine	New York, United States	$924\pm13$	U-Pb ID- TIMS	Krestianinov et al. (2021)
Otter Lake	Quebec, Canada	$913\pm7$	Pb-Pb ID- MC-ICP- MS	Barfod et al. (2005)
Wilberforce	Ontario, Canada	$923\pm14$	U-Pb ID- TIMS	Paul et al. (2021)
Tory Hill	Ontario, Canada	$1021\pm3$	U-Pb ID- TIMS	Fisher et al. (2020a)
OD306	Southern Australia	$1597\pm7$	U-Pb ID- MC-ICP- MS	Thompson et al. (2016)
OD300		$1545\pm20$	U-Pb LA- MC-ICP- MS	Thompson et al. (2016)

<sup>&</sup>lt;sup>a</sup> Reported 2σ uncertainty.

most widely employed U-Pb primary RMs (Tables 1-3) are the McClure, Otter Lake, and Madagascar apatites, but they have limitations. The age of McClure apatite is well-established by multiple TIMS studies (Table 1), but its small grain size (<200 µm-width), low U concentrations (<30 ppm U), and variable amounts of common Pb render it as a sub-optimal primary RM (Krestianinov et al., 2021). Heterogeneous U-Pb ratios in the Otter Lake RM has been shown to result in 1-3% offsets between LA-ICP-MS and isotope dilution (ID) dates for secondary apatite RMs (Thompson et al., 2016). Madagascar apatite megacrysts have internally homogeneous U-Pb isotopic compositions, but can vary significantly between different grains (Table 1; Thomson et al., 2012; Fisher et al., 2020b). Likewise, apatite RMs for Sr and Nd isotopic analyses are limited. In a reconnaissance isotope dilution and laser ablation multi-collector ICP-MS study of Sr and Nd isotopes in 11 different apatite RMs, Yang et al. (2014) concluded that six are homogeneous enough for use as in situ RMs; these are Madagascar, Otter Lake, NW-1, SDG, AP1, and AP2. Since then, Thompson et al. (2016) introduced apatites 401 and OD306 as effective U-Pb RMs (Table 1), but these have vet to be characterized for their Sm-Nd and Sr isotopes. Fisher et al. (2020b) presented Tory Hill apatite from Ontario, Canada, as a viable RM for in situ U-Pb and Nd isotopic analyses (Table 1). More recently, new U-Pb TIMS data for a suite of potential reference apatites from the Adirondack Mountains (Krestianinov et al., 2021) and Wilberforce, Canada (Paul et al., 2021) have been reported (Table 1), but no information on their Sm-Nd or Sr isotopic characteristics are available.

A vital step towards advancing the utility of apatite petrochronology and isotope geochemistry is to expand the suite of available reference materials. In this study, we have characterized the U-Pb, Sr, and Nd isotopic and elemental compositions of two natural apatites from Morocco and Brazil using isotope dilution thermal ionization mass spectrometry (ID-TIMS) and LA-ICP-MS—laser ablation split stream ICP-MS (LASS) for U-Pb and trace-element analyses and more conventional LA-ICP-MS for Sr and Nd isotopes. The prospects and pitfalls of these potential RMs are discussed below.

## 2. Methods

# 2.1. Sample preparation

Multiple untreated, gem-quality apatite crystals from Morocco (MRC) and Brazil (BRZ) were procured online. The former are pale green-yellow crystals from Imilchil, situated within the Triassic–Late Cretaceous Central High Atlas province of Morocco, and the latter are blue crystals derived from Minas Gerais, in the southeastern sector of the Mesoarchean–Paleoproterozoic Brazilian Shield.

A single MRC and BRZ crystal was selected for detailed study (henceforth MRC-1 and BRZ-1). Each crystal had its terminations cut off with a diamond saw and the remaining portions were sliced into mmthick sections parallel to the c-axis (following protocols of Chew et al., 2016) and cast in epoxy (Fig. 1). One mount was analyzed with cathodoluminescence (CL), electron microprobe, ID-TIMS, and LASS/LA-ICP-MS (Fig. 2A, C). Another mount containing additional c-axis parallel sections and a separate c-axis perpendicular piece of the crystal termination (Fig. 2B, D) was analyzed exclusively by LASS to further interrogate intra-crystal U-Pb and elemental heterogeneity.

#### 2.2. Electron microprobe analysis (EPMA)

Cathodoluminescence images of MRC-1 and BRZ-1 crystal sections (Fig. 3) were generated using a FEI Quanta 400f field-emission scanning electron microscope (SEM) equipped with a KE Developments Centaurus CL detector, housed at the University of California, Santa Barbara (UCSB). Quantitative elemental analyses and X-ray maps were collected using a Cameca SX-100 electron probe micro analyzer (EPMA), running Probe for EPMA and Probe Image (Probe Software Inc.), also located at UCSB.

 $<sup>^{\</sup>rm b}$  All apatite analyses unless where noted; MC, multi collector; SC, single collector.

**Table 2**Previously reported Sm-Nd concentrations and isotopic compositions of select apatite RMs.

Apatite	Average Sm [ppm]	Average Nd [ppm]	$^{147}$ Sm/ $^{144}$ Nd $^{a}$	$^{143}$ Nd/ $^{144}$ Nd $^{a}$	Method	References
	182	1322	$\textbf{0.0818} \pm \textbf{5}$	$0.511348\pm16$	ID-MC-ICP-MS	Yang et al. (2014)
MAD	n/a	n/a	$0.0811\pm17$	$0.511322 \pm 53$	LA-MC-ICP-MS	Yang et al. (2014)
	213	1654	$0.0779 \pm 5$	$0.511304\pm13$	ID-TIMS	Fisher et al. (2020b)
	n/a	n/a	$0.0765 \pm 5$	$0.512469 \pm 16$	LA-MC-ICPMS	McFarlane and McCulloch (2008)
	127	1040	$0.0763\pm14$	$0.512449 \pm 10$	LA-MC-ICPMS	McFarlane and McCulloch (2008)
	n/a	n/a	$0.0751\pm25$	$0.512489 \pm 12$	ID-MC-ICP-MS	Fisher et al. (2011)
Dunamaa	n/a	n/a	$0.0785 \pm 58$	$0.512463 \pm 48$	LA-MC-ICPMS	Fisher et al. (2011)
Durango	224	1568	$0.0865\pm17$	$0.512487 \pm 13$	ID-TIMS	Hou et al. (2013)
	n/a	n/a	$0.0852\pm10$	$0.512498 \pm 25$	LA-MC-ICPMS	Hou et al. (2013)
	243	1667	$0.0881\pm11$	$0.512493 \pm 21$	ID-MC-ICP-MS	Yang et al. (2014)
	n/a	n/a	$0.0885\pm19$	$0.512490 \pm 46$	LA-MC-ICPMS	Yang et al. (2014)
M - C1	99	836	$0.0712 \pm 8$	$0.512282 \pm 11$	ID-MC-ICP-MS	Yang et al. (2014)
McClure	n/a	n/a	$0.0696 \pm 72$	$0.512246 \pm 80$	LA-MC-ICP-MS	Yang et al. (2014)

<sup>&</sup>lt;sup>a</sup> Reported weighted mean and 2σ uncertainty.

**Table 3**Previously reported Sr concentrations and isotopic compositions of select apatite RMs

Apatite	Average Sr [ppm]	$^{87}$ Sr/ $^{86}$ Sr $^{a}$	Method	References
MAD	1650	0.71108 ± 3	ID-MC- ICP-MS	Yang et al. (2014)
MAD	n/a	$\begin{array}{c} \textbf{0.71108} \pm \\ \textbf{11} \end{array}$	LA-MC- ICPMS	Yang et al. (2014)
	n/a	$\begin{array}{c} 0.70633 \ \pm \\ 1 \end{array}$	ID-TIMS	Horstwood et al. (2008)
	475	$\begin{array}{c} \textbf{0.70629} \pm \\ \textbf{2} \end{array}$	ID-TIMS	McFarlane and McCulloch (2008)
	n/a	$\begin{array}{c} \textbf{0.70638} \pm \\ \textbf{13} \end{array}$	LA-MC- ICPMS	McFarlane and McCulloch (2008)
Durango	483	$\begin{array}{c} \textbf{0.70634} \pm \\ \textbf{13} \end{array}$	ID-TIMS	Hou et al. (2013)
	n/a	$\begin{array}{c} \textbf{0.70629} \pm \\ \textbf{9} \end{array}$	LA-MC- ICPMS	Hou et al. (2013)
	n/a	$\begin{array}{c} \textbf{0.70633} \pm \\ \textbf{2} \end{array}$	ID-MC- ICP-MS	Yang et al. (2014)
	486	$\begin{array}{c} \textbf{0.70634} \pm \\ \textbf{14} \end{array}$	LA-MC- ICPMS	Yang et al. (2014)
McClure	n/a	$\begin{array}{c} \textbf{0.70369} \pm \\ \textbf{2} \end{array}$	ID-MC- ICP-MS	Yang et al. (2014)
McClure	3422	$\begin{array}{c} \textbf{0.70371}  \pm \\ \textbf{7} \end{array}$	LA-MC- ICPMS	Yang et al. (2014)
BHVO	397	$0.703469 \pm 7$	ID-TIMS	Elburg et al. (2005)
MACS-3	6640	$\begin{array}{l} 0.707553 \\ \pm \ 4 \end{array}$	ID-TIMS	Jochum et al. (2011)

 $<sup>^{\</sup>text{a}}\,$  Reported weighted mean and  $2\sigma$  uncertainty.

X-ray maps were produced using a 20 kV accelerating voltage, 200 nA beam current, and 2- $\mu$ m-diameter beam (Fig. 3). Wavelength-dispersive spectrometers measured Sr and S using LPET crystals, Ce

and Nd using LLIF crystals, and Th using a PET crystal. Maps of MRC-1 and BRZ-1 were developed using a 5  $\mu m$  by 5  $\mu m$  pixel spacing and 3  $\mu m$  by 3  $\mu m$  pixel spacing, respectively, all using a dwell time of 500 ms per pixel.

Quantitative EPMA 'spots analyses' were acquired with an accelerating voltage of 20 kV, a beam current of 200 nA and a 5-µm-diameter defocused beam. The location of the spot transects are shown in Fig. 2. X-ray intensity measurements were made for La, Ce, Nd, Pr, Si, Na, Th, Gd, Sm, Sr, Y, and S using wavelength-dispersive spectrometers. A series of natural and synthetic standards were analyzed, including: ThO $_2$  for Th ma, strontium titanate (SrTiO $_3$ ) for Sr la, Cazadero albite for Si ka, Na ka, anhydrite (CaSO $_4$ ) UC # 5555 for S ka, Edinburgh REE Glass for Y la, La la, Ce la, Pr l $_3$ , Nd la, Sm l $_3$ , and Gd la. The full EPMA dataset is reported in Supplementary Table S3 and representative averages are reported in Table 4.

#### 2.3. U-Pb ID-TIMS

Seven  $\sim$ 0.1 mg fractions were taken from the MRC-1 apatite, and eight  $\sim$ 0.3 mg fractions from the BRZ-1 crystal were separated at Boise State University using a diamond saw. Approximate locations shown as yellow circles in Fig. 2. In the case of the MRC-1 crystal, different growth zones were targeted to assess potential intra-crystal heterogeneity. For the BRZ-1 apatite, seven fragments were separated from the interior of the crystal, away from CL-bright cracks, and one fragment was separated from near the rim for comparison.

All apatite crystal fragments were cleaned in an ultrasonic ethanol bath. The fragments were then spiked with an enriched  $^{205}\text{Pb-}^{233}\text{U-}^{235}\text{U}$  tracer (BSU-1B calibrated against EARTHTIME gravimetric standards), and dissolved in concentrated HF at 220 °C for 48 h in PFA fluoropolymer capsules nested within PTFE fluoropolymer-lined high-pressure steel dissolution vessels. After dissolution, drying to salts, and re-

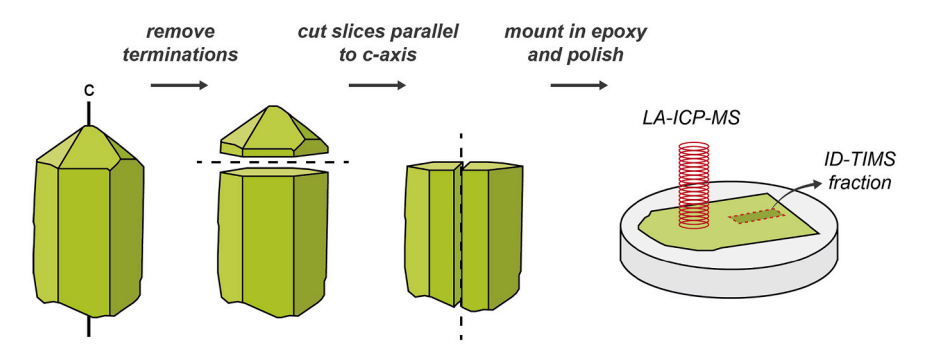
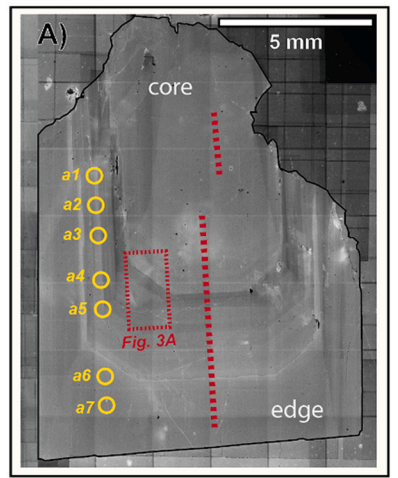


Fig. 1. Cartoon of specimen preparations (following recommendations of Chew et al., 2016). Crystal terminations are sawn off, and the remaining prism is cut along its c-axis into mm-thick slices. In this study, a crystal section was analyzed using CL, EPMA, LASS/LA-ICP-MS, and ID-TIMS. An additional crystal section was analyzed by LASS to assess chemical heterogeneity (Fig. 2B and D).

# MRC-1 Mount 1



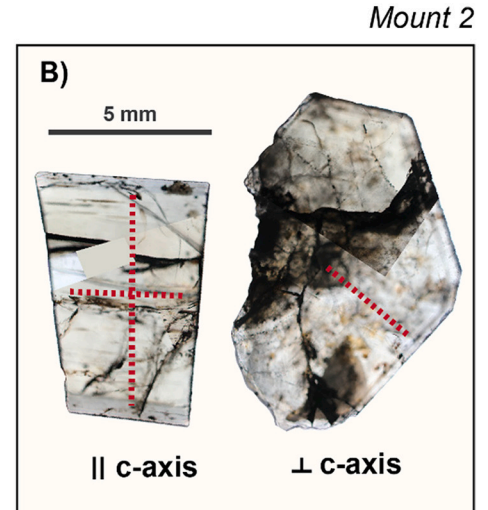
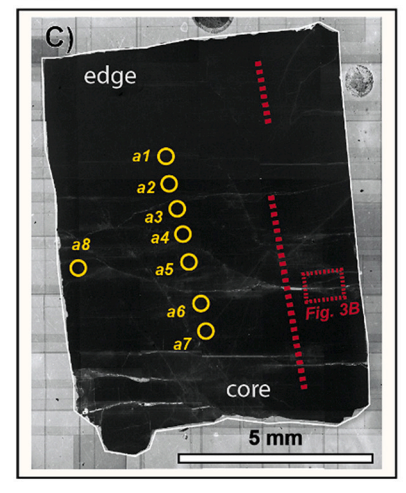
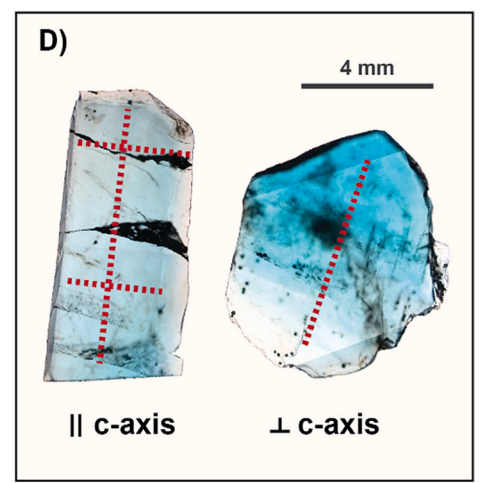


Fig. 2. Left) CL maps of MRC-1 showing zonation and of BRZ-1 showing conspicuous cracks (white/grey wisps). Yellow circles indicate location of extracted TIMS fractions. Red dashed lines are approximate trajectories of LASS transects. Red dashed rectangles represent location of EPMA maps shown in Fig. 3. Right) photomicrographs of additional c-axis parallel and perpendicular sections analyzed by LASS. Red dashed lines are approximate LASS paths. (For interpretation of the references to color in this figure legend, the reader is referred to the web version of this article.)

# BRZ-1





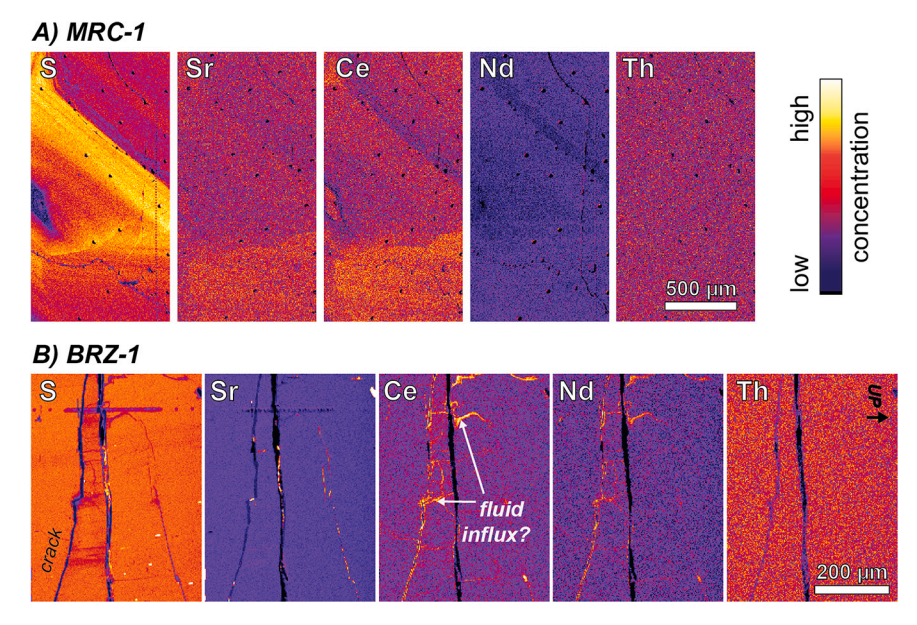


Fig. 3. Qualitative X-ray maps of apatites. A) Zoning in MRC-1 is marked by differences in S, Sr, Ce, and Nd (no significant Th variation is captured by EPMA). B) Areas near cracks in BRZ-1 are compositionally distinct from the matrix (enriched in Ce and Nd relative to the matrix). Color scale on each map is qualitative and the colors were edited to emphasize contrast; warmer colors indicate higher concentrations relative to cooler colors.

Table 4

Average trace element concentrations determined by EPMA (full data set in Supplementary Table S1).

EMPA transect		La	Ce	Nd	Pr	Si	Na	Th	Gd	Sm	Sr	Y	S
		[ppm]	[ppm]	[ppm]	[ppm]	[ppm]	[ppm]	[ppm]	[ppm]	[ppm]	[ppm]	[ppm]	[ppm]
BRZ-1													
20 $\mu$ m line scan ( $n=30$ )	Av.	368.0	623.5	336.1	b.d.l	4054.2	408.5	813.7	79.3	b.d.l	292.2	136.9	3224.3
20 $\mu$ m mie scan ( $n = 30$ )	1SD	59.6	114.3	46.5	b.d.l	82.8	38.6	51.6	34.8	b.d.l	21.3	29.3	173.0
F line com 1 (n 62)	Av.	313.0	656.9	251.4	b.d.l	3729.1	446.7	809.5	71.9	b.d.l	311.8	143.9	3315.3
5 $\mu$ m line scan 1 ( $n = 63$ )	1SD	95.8	160.9	70.9	b.d.l	289.8	79.5	108.1	36.6	b.d.l	43.2	34.6	394.5
F lime coon 2 (m. 24)	Av.	287.2	604.6	260.3	b.d.l	3809.8	430.0	770.3	66.3	b.d.l	298.5	134.7	3168.5
5 $\mu$ m line scan 2 ( $n = 24$ )	1SD	79.4	78.1	78.3	b.d.l	226.9	77.9	73.2	33.5	b.d.l	32.9	28.7	259.8
F lime coon 2 (m. 112)	Av.	321.3	690.0	264.0	b.d.l	3823.9	488.0	723.3	82.5	b.d.l	294.7	144.2	3160.5
5 $\mu$ m line scan 3 ( $n = 113$ )	1SD	85.2	120.8	70.7	b.d.l	324.1	100.7	111.7	38.1	b.d.l	31.1	30.1	278.0
-11 (	Av.	321.5	663.4	269.6	b.d.l	3829.0	459.9	762.3	77.6	b.d.l	299.3	142.1	3209.2
all scans ( $n=230$ )	1SD	86.9	131.7	73.4	b.d.l	299.7	91.1	109.1	37.0	b.d.l	34.5	31.1	304.7
MRC-1													
20 1:	Av.	2456.9	3708.4	1487.4	302.6	3206.7	470.2	364.0	587.6	b.d.l	823.1	1454.5	1276.3
20 $\mu$ m line scan ( $n = 147$ )	1SD	179.7	267.4	100.1	75.9	389.1	73.7	68.9	62.1	b.d.l	41.9	89.2	274.2

b.d.l., below detection limit. Averages discarded outliers beyond 2SD.

equilibration in 6 M HCl at  $180\,^{\circ}\text{C}$  for  $12\,\text{h}$ , Pb and U were separated from the solutions using dilute HBr- and HCl-based anion exchange chromatography (Krogh, 1973).

The U-Pb aliquots were loaded in a silica gel emitter (Gerstenberger and Haase, 1997) to outgassed, zone-refined Re filaments. Isotopic determinations were performed using an IsotopX PhoeniX-62 TIMS. A correction for mass-dependent Pb fractionation was applied based on repeated measurements of NBS 982 (Catanzaro et al., 1968) Pb on both the Daly ion counter [0.16 ( $\pm$  0.03%) amu–1; 1 s] and the Faraday cups [0.10  $\times$  (1  $\pm$  0.02%) amu–1; 1 s]. Uranium was run as an oxide (UO2) and measured in static mode on Faraday detectors equipped with 1012  $\Omega$  resistors. The U mass fractionation for the same analyses was calculated using the  $^{233}\text{U}/^{235}\text{U}$  ratio of the double spike solution (0.99506%  $\pm$  0.01%, 1 s).

The U-Pb dates and uncertainties for each analysis were calculated using the algorithms of Schmitz and Schoene (2007), the U decay constants of Jaffey et al. (1971), and a value of  $^{238}U/^{235}U = 137.88$ . Uranium oxide measurements were corrected for isobaric interferences using an <sup>18</sup>O/<sup>16</sup>O value of 0.00206. Uncertainties are based upon random analytical errors, including counting statistics, instrumental fractionation, tracer subtraction, and blank subtraction. Non-radiogenic Pb was attributed to laboratory blank (~0.5 pg, determined by total procedural blanks measurements) and intrinsic common Pb in the apatite (compositions estimated from LA data or assuming a model Pb composition from Stacey and Kramers (1975), discussed below). These error estimates should be considered when comparing our  $^{206}\text{Pb}/^{238}\text{U}$ dates with those from other laboratories that used tracer solutions calibrated against the EARTHTIME gravimetric standards. When comparing our dates with those derived from other decay schemes (e.g., <sup>40</sup>Ar/<sup>39</sup>Ar, <sup>187</sup>Re-<sup>187</sup>Os), the uncertainties in tracer calibration (0.03%; Condon et al., 2015; McLean et al., 2015) and U decay constants (0.108%; Jaffey et al., 1971) should be added to the internal error in quadrature. Quoted errors for calculated weighted means are in the form  $\pm$  X (Y) [Z], where X is solely analytical uncertainty, Y is the combined analytical and tracer uncertainty, and Z is the combined analytical, tracer, and  $^{238}$ U decay constant uncertainty. The U-Pb TIMS dataset is reported in Table S4.

#### 2.4. Sm-Nd and Sr ID-TIMS

Six TIMS aliquots from each apatite were further processed for Sm-Nd and Sr isotopic measurements. Washes from apatite crystal fragments dissolved and separated for U-Pb were spiked with mixed  $^{149}\rm Sm^{-}^{150}\rm Nd$  and  $^{87}\rm Rb^{-}^{84}\rm Sr$  tracers, dried, and re-dissolved in 5 mL 1 M HCl + 0.1 M HF at 120 °C overnight. Sr and bulk rare earth elements were separated by standard dilute HCl- and HNO<sub>3</sub>-based cation exchange chemistry on 6 mm inner diameter (i.d.) x 20 cm long columns of

AG-50 W-X8 resin (H+ form, 200–400 mesh). Sr was further purified by loading on 0.05 mL c.v. of Sr-spec crown ether resin and elution of matrix elements with 1.3 mL 3.5 M HNO $_3$ , followed by elution of Sr in ultrapure water. Sm and Nd were separated by reverse phase HDEHP chromatography on 4 mm i.d. x 10 cm long columns of Eichrom Ln-spec resin, 50–100 mesh. All separated fractions were dissolved and re-dried with 30 mL16M HNO $_3$ , 30 mL 30% H $_2$ O $_2$ , and 5 mL 0.1 N H $_3$ PO $_4$ .

The Nd fraction was loaded in 2 mL of 1 M HNO<sub>3</sub> on the side filament of a triple Re filament assembly, whereas the Sm fraction was loaded on a single Re filament in 2 mL 1 M HNO<sub>3</sub> along with 3 mL of tantalum oxide emitter solution. Sm and Nd isotopes were measured on an IsotopX Phoenix X62 multi-collector thermal ionization mass spectrometer in static and dynamic Faraday modes, respectively. Instrumental mass fractionation of Sm and Nd isotopes was corrected with an exponential law relative to  $^{146}\text{Nd}/^{144}\text{Nd}=0.7219$  and  $^{152}\text{Sm}/^{147}\text{Sm}=1.7831$ . The quoted uncertainty for each analysis is the internal standard error; the external reproducibility (standard deviation) of the JNdi-1 standard over the course of the study was  $0.512105\pm4$  (2 $\sigma$ ) for runs at  $\sim$ 3 V  $^{144}\text{Nd}$  (n=8) and  $0.512105\pm8$  (2 $\sigma$ ) for runs at  $\sim$ 0.3 V  $^{144}\text{Nd}$  (n=9). Uncertainty in [Sm], [Nd], and  $^{147}\text{Sm}/^{144}\text{Nd}$  are estimated at  $\leq$ 0.022% (2 $\sigma$ ), including systematic tracer calibration errors.

The Sr fraction was loaded in 2 mL 1 M HNO $_3$  along with 3 mL of tantalum oxide emitter solution on single degassed Re filaments, and its isotope ratios measured on the IsotopX Phoenix X62 multi-collector TIMS in the Boise State University Isotope Geology Laboratory. Sr isotope ratios were analyzed in dynamic mode, fractionation-corrected with an exponential law relative to  $^{86}$ Sr/ $^{88}$ Sr = 0.1194. The quoted uncertainty for each analysis is the internal standard error; the external reproducibility of the NBS-987 standard over the course of the study was 0.710244  $\pm$  6 (2 $\sigma$ ) for runs at 4 V  $^{88}$ Sr (n = 7). The TIMS Sm-Nd and Sr isotopic data are presented in Table S5.

#### 2.5. U-Pb and trace element LASS

Combined U-Pb and trace-element data were collected using the LASS system at UCSB during different sessions over a two-year period. The system consists of a Photon Machines 193 nm excimer Analyte laser with a HelEx-2 ablation cell coupled to two mass spectrometers: a MC-ICP-MS for U-Pb isotopes and a quadrupole (Q)-ICP-MS for simultaneous trace element determinations (see also Kylander-Clark et al., 2013). A Nu Instruments Plasma 3D MC-ICP-MS was used for the first phase of the study, and a Nu Instruments Plasma HR-ES MC-ICP-MS for the second phase. An Agilent 7700S Q-ICP-MS was untilized for all trace-element analyses. Instrument parameters are summarized in Table 5. On the Plasma 3D MC-ICP-MS,  $^{202}{\rm Hg}, ^{204}{\rm (Pb} + {\rm Hg}), ^{206}{\rm Pb}, ^{207}{\rm Pb}, ^{208}{\rm Pb}$  were measured on Daly detectors and  $^{238}{\rm U}$  and  $^{232}{\rm Th}$  were measured on Faraday collectors; similarly,  $^{204}{\rm (Pb} + {\rm Hg}), ^{206}{\rm Pb}, ^{207}{\rm Pb}, ^{208}{\rm Pb}$  were

Table 5
ICP instrument parameters for U-Pb/TE, Sm-Nd, and Sr isotopic analyses.

Instruments								
Instrument model	Nu Instruments Plasma 3D MC-ICP-MS	Nu Instruments Plasma HR-ES MC-ICP-MS	Agilent 7700S quadrapole					
RF power	1300 W	1300 W						
Make-up gas flow	0.7–0.8 L/min (U-Pb TE LASS) 1.07 L/min (Sm-Nd, Sr)	0.7–0.8 L/min (U-Pb TE LASS)	1.4 L/min (U-Pb TE LASS)					
Masses measured	$ \mbox{U-Pb} + \mbox{TE LASS:} \ ^{204}\mbox{Hg} + \mbox{Pb,} \ ^{206,207,208}\mbox{Pb on SEMs;} \ ^{232}\mbox{Th,} \ ^{238}\mbox{U} \label{eq:u-Pb} $ on Faraday cups	U-Pb + TE LASS: <sup>202</sup> Hg, <sup>204</sup> Hg + Pb, <sup>206,207,208</sup> Pb on SEMs; <sup>232</sup> Th, <sup>238</sup> U on Faraday cups	$\begin{array}{l} \text{U-Pb} + \text{TE LASS:}  ^{44}\text{Ca},  ^{88}\text{Sr},  ^{89}\text{Y},  ^{90}\text{Zr},  ^{139}\text{La}, \\ ^{140}\text{Ce},  ^{141}\text{Pr},  ^{146}\text{Nd},  ^{147}\text{Sm},  ^{153}\text{Eu},  ^{157}\text{Gd},  ^{159}\text{Tb}, \\ ^{163}\text{Dy},  ^{165}\text{Ho},  ^{166}\text{Er},  ^{169}\text{Tm},  ^{172}\text{Yb},  ^{175}\text{Lu} \pm ^{49}\text{Ti} \pm \end{array}$					
	$\begin{split} &\text{Sm-Nd: } ^{142}\text{Nd, } ^{143}\text{Nd, } ^{144}\text{Nd} + \text{Sm, } ^{145}\text{Nd, } ^{146}\text{Nd, } ^{147}\text{Sm, } ^{148}\text{Nd, } \\ ^{149}\text{Sm, } ^{150}\text{Nd on Faraday cups} \\ &\text{Sr. } ^{82}\text{Kr^+} + (^{164}\text{Er^{++}}) + (^{40}\text{Ca}^{42}\text{Ca}), ^{167}\text{Er^{++}}, \\ ^{84}\text{Sr^+} + \text{Kr^+} + (^{168}\text{Yb^{++}} + \text{Er^{++}}), ^{85}\text{Rb^{+}} + (^{170}\text{Yb^{++}} + \text{Er^{++}}), \\ ^{86}\text{Sr^+} + \text{Kr^+} + (^{172}\text{Yb^{++}}), ^{173}\text{Yb^{++}}, ^{87}\text{Sr^{+}} + \text{Rb^{+}} + (^{174}\text{Yb^{++}}), \\ ^{175}\text{Lu^{++}}, ^{88}\text{Sr^{+}} + (^{176}\text{Lu^{++}} + \text{Yb^{++}}) + (^{40}\text{Ca}^{48}\text{Ca}) \text{ on Faraday cups} \end{split}$		$^{55}$ Mn $\pm$ $^{56}$ Fe $\pm$ $^{137}$ Ba					
Integration time per peak/dwell times; quadrupole sweep time	100 ms	500 ms	~200 ms					
Total integration (sweep) time per output data point	0.5 s	0.5 s	0.5 s					
Laser ablation system Make, Model and type Ablation cell and volume Laser wavelength Pulse width Fluence; pit depth/pulse Repetition rate Ablation duration Spot diameter Sampling mode / pattern Carrier gas Cell carrier gas flow	Cetac Teledyne 193 nm excimer Analyte laser  HelEx-2 ablation cell (Eggins et al., 1998; Eggins et al., 2005) 193 nm 4 ns ~1 J/cm²; ~0.08–0.1 µm/pulse 4 Hz (U-Pb + TE LASS), 15 Hz (Sm-Nd, Sr); 15 s (U-Pb + TE LASS), 20 s (Sm-Nd, Sr) 40 µm (U-Pb + TE LASS), 50 µm + 85 µm (Sm-Nd, Sr) Static spot ablation 100% He in the cell, Ar make-up gas combined in a glass mixing 0.15 L/min total (0.12 L/min for cup, 0.03 L/min for cell)	y bulb						
Data Processing Reference Materials Data processing package Common-Pb correction, composition and uncertainty	No common-Pb correction applied to the data; the $2\sigma$ uncertainty 0.5 for Stacey-Kramers model common-Pb	see Tables 1–3 Iolite v. 2.5 (Paton et al., 2011); LIEF correction assumes reference material and samples behave identically. No common-Pb correction applied to the data; the $2\sigma$ uncertainty of $(^{207}\text{Pb}/^{206}\text{Pb})_i$ determined by linear regression through U-Pb data or assumed to be						
Uncertainty level and propagation	Ages are quoted at 2 s absolute, propagation is by quadratic add composition uncertainty are propagated where appropriate.	ition. Reproducibility and age unce	ertainty of reference material and common-Pb					

measured on Secondary Electron Multipliers and  $^{238}U$  and  $^{232}Th$  were measured on Faraday collectors on the Plasma HR. On the Q-ICP-MS, the following masses were measured:  $^{28}\text{Si},\,^{44}\text{Ca},\,^{88}\text{Sr},\,^{89}\text{Y},\,^{90}\text{Zr},\,^{139}\text{La},\,^{140}\text{Ce},\,^{141}\text{Pr},\,^{146}\text{Nd},\,^{147}\text{Sm},\,^{153}\text{Eu},\,^{157}\text{Gd},\,^{159}\text{Tb},\,^{163}\text{Dy},\,^{165}\text{Ho},\,^{166}\text{Er},\,^{169}\text{Tm},\,^{172}\text{Yb},\,^{175}\text{Lu} \pm\,^{49}\text{Ti} \pm\,^{55}\text{Mn} \pm\,^{56}\text{Fe} \pm\,^{137}\text{Ba}.$ 

Apatite was ablated using a 40- $\mu$ m-diameter laser spot operating at a 4 Hz repetition rate, 50% of 5 mJ laser power, and a laser fluence of  $\sim$ 1 J/cm2. Each ablation sequence consisted of two cleaning shots, followed by 20 s of monitored washout and 15 s of ablation, equating to final pit depths of  $\sim$ 7  $\mu$ m. Raw U-Pb ratios were baseline subtracted and corrected for laser- and plasma-induced element fractionation, and instrument drift using the Iolite software package (v. 2.5; Paton et al., 2011) in the Igor Pro interactive software environment (or Iolite as a shorthand).

Apatite RM MAD—denoted here as MAD-UCSB, an apatite crystal from Madagascar provided by Stuart Thompson and subsequently analyzed via ID-TIMS at the Boise State Isotope Geology Lab for this study—served as the primary bracketing reference apatite for LASS analyses. All of the analyzed fractions of MAD-UCSB have homogeneous U-Pb ratios (Fig. 4), and we adopted the weighted mean and associated  $2\sigma$  error of the data as the canonical U-Pb isotopic compositions for LASS standardization. Details of this RM are reported in section 3.2.

All of the secondary apatite RMs contain variable amounts of common-Pb, so the U-Pb age quoted herein is the concordia intercept age determined from a York regression through the data. Repeat analyses of secondary RMs over the course of this study indicate that each  $^{238}\mathrm{U}/^{206}\mathrm{Pb}$  and  $^{207}\mathrm{Pb}/^{206}\mathrm{Pb}$  measurements require an additional 2.4% and 1.8% (2 $\sigma$ ), respectively, to account for the long-term variability in

laser ablation analyses; these values were added in quadrature to the internal error of each U-Pb datum and considered when calculating intercept ages (Horstwood et al., 2016). Final U-Pb ratios and associated uncertainties were plotted using IsoplotR (Vermeesch, 2018). The concordia intercept ages of the secondary RMs overlap their established ages with these designated uncertainties (Table 6).

Trace-element abundances in apatite were calculated in Iolite using  $^{44}$ Ca as the internal standard element and assuming stoichiometric abundances of Ca in fluoroapatite (39.74%). The NIST 612 silicate glass (Pearce et al., 1997) was used for calibration (preferred values of Jochum et al., 2011). The uncertainty of each element reflects only the internal error. The complete LASS data set is presented in Supplementary Table S6.

## 2.6. Sm-Nd LA-MC-ICP-MS

Isotopes of Sm-Nd were measured using a Photon Machines 193 nm excimer Analyte laser with a HelEx-2 ablation cell coupled to a Nu Instruments Plasma 3D MC-ICP-MS. Masses 140–158 were measured on 16 Faradays collectors at 1-amu spacing (Table 5); detector configurations are presented in Supplementary Table S9. Apatite was ablated for 300 laser pulses using a 15 Hz repetition rate at 100% of 5 mJ laser power during two consecutive sessions: one utilizing a 50- $\mu$ m-diameter spot and the other an 85- $\mu$ m-diameter spot. Each ablation sequence consisted of two cleaning shots, followed by 50 s of monitored washout, 20 s of ablation—amounting to final pit depths of 20–22  $\mu$ m—and 3 s of wash out prior to the next sequence.

## Madagascar apatite

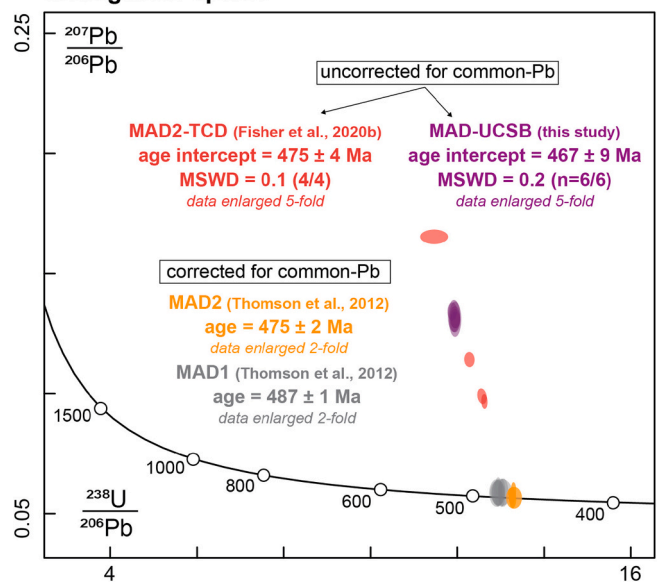


**Fig. 4.** Tera-Wasserburg concordia diagram of Madagascar apatite data (Thomson et al., 2012; Fisher et al., 2020b; this study). MAD-UCSB and MAD2-TCD data are common-Pb uncorrected (MAD2-TCD data from *C. Fisher*, personal communication) whereas MAD1 and MAD2 are common-Pb corrected. Different MAD crystals have distinct U-Pb ratios, highlighting inter-crystal heterogeneity for this RM. Note that the data are enlarged for visualization.

Mass bias, isobaric interferences, and laser-induced (downhole) fractionation can be significant sources of uncertainty and must be corrected for in order to obtain accurate 143Nd/144Nd and 147Sm/144Nd measurements by LA-MC-ICP-MS (e.g., Vance and Thirlwall, 2002; Fisher et al., 2011, 2020b). Our approach to these corrections follows that of Fisher et al. (2011) and Poletti et al. (2016) and is summarized below. Mass-bias correction for Sm was based on internal standardization using the natural ratio of <sup>147</sup>Sm/<sup>149</sup>Sm (0.22332; Isnard et al., 2005). The isobaric interference of <sup>144</sup>Sm on <sup>144</sup>Nd was calculated using the calculated mass bias and assuming a natural ratio of  $^{144}$ Sm/ $^{149}$ Sm = 1.08680 (Dubois et al., 1992). For Nd isotopes, mass-bias correction was based on the natural ratio of  $^{146}$ Nd/ $^{144}$ Nd = 0.7219. All of these corrections—as well as baseline subtractions and corrections for instrumental drift-were done in Iolite (v. 3.5) using the Sm-Nd data reduction scheme developed by Fisher et al. (2020b). Downhole corrections to the mass-bias- and interference-corrected  $^{147}\mathrm{Sm}/^{144}\mathrm{Nd}$  and <sup>143</sup>Nd/<sup>144</sup>Nd ratios were made using an exponential fit and using MAD-UCSB as the primary RM (using <sup>147</sup>Sm/<sup>144</sup>Nd and <sup>143</sup>Nd/<sup>144</sup>Nd compositions determined by TIMS as part of this study; Table 7). Secondary reference apatites analyzed during each run include McClure, Durango, OD306, and 401 (Table 3). Reported uncertainties are 2σ and only include in-run errors; for both the 50 and 85 μm diameter spot analyses, repeated analyses of secondary RMs yielded weighted means with MSWDs that are consistent with a uniform population (Wendt and Carl, 1991), the exceptions being Durango and OD306. These latter two RMs are known to exhibit Nd isotopic heterogeneity (Fisher et al., 2011; Yang et al., 2014) or have not yet been characterized for their Sm-Nd systematics by TIMS analyses. The complete Sm-Nd isotopic data set is presented in Supplementary Table S7.

#### 2.7. Sr LA-MC-ICP-MS

Multiple isobaric interferences can impair Sr isotopic measurements by LA-MC-ICP-MS, including Kr in the carrier He gas and plasma Ar gas, doubly-charged REEs—e.g., Er<sup>2+</sup> and Yb<sup>2+</sup>—and Ca-dimers from the apatite matrix (e.g., Ramos et al., 2004; Horstwood et al., 2008). Sr isotopes were measured at UCSB using the same set up described above for Sm-Nd analyses. The detector array covered masses 81.5–89.5 with a 0.5-amu spacing; all measurements were made on Faraday collectors (see Supplementary Table S10 for detector array configuration). These laser ablation analyses were completed in two consecutive sessions, the first using an 85-µm-diameter spot and the second a 50-µm-diameter spot (Table 5). Laser settings and ablation sequences used for Sr analyses are the same as described for our Sm-Nd isotopic analyses except that a 50 s baseline was collected following the main ablation pass (i.e., a single sequence consisted of two cleaning shots, 50 s baseline, 20 s ablation pass, and 50 s baseline).

Accurate Sr isotopic determinations are dependent not only on corrections for isobaric interferences, but also the order in which corrections are applied (e.g., Horstwood et al., 2008; Yang et al., 2014). First, given the relatively long baseline before and after each ablation pass (50 s each), <sup>86,84,82</sup>Kr<sup>+</sup> interferences were subtracted using a step-forward baseline subtraction (Bizzarro et al., 2003). Following this, interferences from various doubly-charged REEs on Sr and Rb isotopes and Ca-dimers were calculated—<sup>176</sup>Yb<sup>2+</sup> and <sup>176</sup>Lu<sup>2+</sup> on <sup>88</sup>Sr, <sup>174</sup>Yb<sup>2+</sup> on <sup>87</sup>Sr, <sup>172</sup>Yb<sup>2+</sup> on <sup>86</sup>Sr, <sup>170</sup>Yb<sup>2+</sup> and <sup>170</sup>Er<sup>2+</sup> on <sup>85</sup>Rb (used for <sup>87</sup>Rb corrections on <sup>87</sup>Sr), <sup>168</sup>Yb<sup>2+</sup> and <sup>168</sup>Er<sup>2+</sup> on <sup>84</sup>Sr, and <sup>164</sup>Er<sup>2+</sup> and <sup>164</sup>Dy<sup>2+</sup> on mass-82. Each REE interference intensity was calculated using the mass bias derived from the measured <sup>86</sup>Sr/<sup>88</sup>Sr (low REE concentrations across the apatite RMs prevented determinations of mass bias factors for individual REEs). Interferences from Er isotopes were computed using

**Table 6**Summary of U-Pb age results from this study.

Apatite	Method	Average U [ppm]	Average Th [ppm]	Intercept age (Ma) <sup>a</sup>	$(^{207}\text{Pb}/^{206}\text{Pb})_{i}$	Common-Pb correction
MAD-UCSB	ID-TIMS	22	545	$467.4 \pm 8.4$	$0.71 \pm 0.10$	Total Pb-U
	ID-TIMS	31	285	$153.4\pm0.4$	$0.85\pm0.04$	Total Pb-U
				$153.5\pm0.4$	$0.86\pm0.08$	unanchored York regression
MRC-1				$153.4\pm0.4$	$0.85\pm0.05$	Stacey-Kramers (153 Ma)
	LASS	34	330	$152.7\pm0.6$	$0.85\pm0.04$	Total Pb-U ( <sup>207</sup> Pb/ <sup>206</sup> Pb) <sub>i</sub>
				$152.8\pm0.9$	$0.85\pm0.05$	Stacey-Kramers (153 Ma)
	ID-TIMS <sup>b</sup>	65	892	$2078\pm12$	$1.14 \pm 0.09$	Total Pb-U
				$2077 \pm 14$	$1.13\pm0.08$	unanchored York regression
DD7 1				$2069 \pm 11$	$1.01\pm0.05$	Stacey-Kramers (153 Ma)
BRZ-1	LASS	76	879	$2038\pm14$	$1.14 \pm 0.09$	Total Pb-U ( <sup>207</sup> Pb/ <sup>206</sup> Pb) <sub>i</sub>
				$2042\pm12$	$1.06\pm0.06$	unanchored York regression
				$2038\pm11$	$1.01\pm0.05$	Stacey-Kramers (153 Ma)
Durango	LASS	15	339	$29.4\pm1.2$	$0.84 \pm 0.05$	Stacey-Kramers (31 Ma)
McClure	LASS	17	43	$517.0 \pm 8.0$	$0.87\pm0.04$	unarchored York regression
401	LASS	17	125	$508.4 \pm 5.7$	$0.66\pm0.30$	unarchored York regression
OD306	LASS	23	64	$1570\pm15$	$1.5\pm1.1$	unarchored York regression

<sup>&</sup>lt;sup>a</sup> 2σ, in-run errors with propogated long-term uncertainties (LASS) and tracer uncertainties (ID-TIMS).

<sup>&</sup>lt;sup>b</sup> Includes only 3/8 cogenetic points.

Chemical Geology 590 (2022) 120689

Table 7

F.E. Apen et al.

Apatite	Method	Average Sm [ppm]	Average Nd [ppm]	Average <sup>147</sup> Sm/ <sup>144</sup> Nd <sup>a</sup>	Average <sup>143</sup> Nd/ <sup>144</sup> Nd
	ID-TIMS LA-ICP-	165	1283	$0.07763\pm4$	0.511312 ± 3
MAD- UCSB	MS (50 μm)	185	1514	$0.07799 \pm 4$	$\begin{array}{c} 0.511310 \; \pm \\ 32 \end{array}$
	LA-ICP- MS (85 µm)	285	1513	$0.07800\pm9$	$\begin{array}{c} 0.511309 \ \pm \\ 26 \end{array}$
	ID-TIMS LA-ICP-	206	1136	$0.10923 \pm 9$	$0.512677 \pm 3$
	MS (50 μm)	284	1541	$0.11717\pm3$	$0.512710 \pm 18$
MRC-1	LA-ICP- MS (85 μm)	285	1550	$\textbf{0.11674} \pm \textbf{5}$	$\begin{array}{c} \textbf{0.512689} \pm \\ \textbf{13} \end{array}$
WING-1	ID-TIMS	24	143	$0.10152\pm 8$	0.510989 ±
	LA-ICP- MS (50 μm)	42	267	$0.09854 \pm 5$	$\begin{array}{c} \textbf{0.510994} \pm \\ \textbf{70} \end{array}$
BRZ-1	LA-ICP- MS (85 μm)	42	266	$0.09981 \pm 6$	$\begin{array}{c} \textbf{0.510887} \pm \\ \textbf{46} \end{array}$
	LA-ICP- MS (50 μm) LA-ICP-	189	1381	$0.08760 \pm 20$	$\begin{array}{c} \textbf{0.512485} \pm \\ \textbf{34} \end{array}$
Durango	MS (85 μm) LA-ICP-	192	1397	$0.08720\pm10$	$\begin{array}{c} \textbf{0.512470} \pm \\ \textbf{24} \end{array}$
	MS (50 μm) LA-ICP-	114	963	$0.07420 \pm 48$	$\begin{array}{l} 0.512351 \; \pm \\ 46 \end{array}$
McClure	MS (85 μm) LA-ICP-	120	1027	$0.07180\pm47$	$\begin{array}{c} \textbf{0.512266} \pm \\ \textbf{32} \end{array}$
	MS (50 μm) LA-ICP-	421	3007	$\textbf{0.08920} \pm 1$	$\begin{array}{c} \textbf{0.512282} \pm \\ \textbf{22} \end{array}$
401	MS (85 μm)	434	3070	$0.09050\pm4$	$\begin{array}{c} \textbf{0.512282} \pm \\ \textbf{16} \end{array}$
	LA-ICP- MS (50 μm)	346	2734	$0.08060 \pm 5$	$\begin{array}{c} \textbf{0.511238} \pm \\ \textbf{22} \end{array}$
OD306	LA-ICP- MS (85 µm)	331	2650	$0.07870 \pm 42$	$0.511212 \pm 16$

<sup>&</sup>lt;sup>a</sup> Weighted mean and associated 2σ uncertainty; age uncorrected.

the 167Er signal at the 83.5 half-mass and the natural ratios of Er isotopes:  $^{170}\text{Er}/^{167}\text{Er} = 0.65111$ ,  $^{168}\text{Er}/^{167}\text{Er} = 1.16790$ , and  $^{164}\text{Er}/^{167}\text{Er} =$ 0.04779. Similarly, Yb interferences were calculated with the <sup>173</sup>Yb half mass and the natural ratios of Yb isotopes:  ${}^{176}\text{Yb}/{}^{173}\text{Yb} = 0.79107$ .  $^{174}$ Yb/ $^{173}$ Yb = 1.97702,  $^{172}$ Yb/ $^{173}$ Yb = 1.35338,  $^{170}$ Yb/ $^{173}$ Yb = 0.18847, and  $^{168}\text{Yb}/^{173}\text{Yb} = 0.00806$ . For the  $^{176}\text{Lu}^{2+}$  interference, we employed the measured <sup>175</sup>Lu half mass and the natural ratio of  $^{176}$ Lu/ $^{175}$ Lu = 0.02659. The  $^{164}$ Dy interference was calculated using  $^{163}$ Dy (at the 81.5 half mass) using a natural ratio of  $^{164}$ Dy/ $^{163}$ Dy = 1.13173. Rare-earth-element corrections were first applied to mass-82, and the residual signal was assumed to correspond entirely to <sup>40</sup>(Ca, Ar)<sup>42</sup>Ca (see also Horstwood et al., 2008); this value was used to estimate Ca-dimer interferences on masses 84-88 by applying natural Ca abundances. Given the similar relative isotopic abundances of  $^{40}$ Ca and <sup>40</sup>Ar, we assumed that interferences from Ca-argides were also accounted for in correcting for the Ca-dimers (Horstwood et al., 2008). Interferences from REEs and Ca-dimers were stripped to ascertain <sup>84,86,87,88</sup>Sr and <sup>85</sup>Rb, the latter of which was used to compute and subtract the final interference of <sup>87</sup>Rb on <sup>87</sup>Sr based on an <sup>87</sup>Rb/<sup>85</sup>Rb ratio = 0.38561.

Baseline subtractions and drift-corrections, as well corrections for

the isobaric interferences listed above, were carried out in Iolite. Apatite RMs MAD-UCSB, McClure, Durango, OD306, and 401, United States Geological Survey (USGS) silicate glass BHVO-2G and USGS carbonate MACS-3 were analyzed during the run to monitor the accuracy and precision of the final Sr isotopic analyses (Table 3). Additional uncertainties derived from repeat analyses of each RM were propagated to the REE-, Ca-dimer, and Rb-corrected  $^{87}\mathrm{Sr}/^{86}\mathrm{Sr}$  internal error ( $\sim\!0.02\%$ ;  $2\sigma$ ). Final  $^{87}\mathrm{Sr}/^{86}\mathrm{Sr}$  values were not standardized. The complete Sr isotopic data set is presented in Supplementary Table S8.

#### 3. Results

#### 3.1. CL and EPMA

Quantitative X-ray maps and CL imaging reveal internal structures and provide a basis for interpreting potentially complex dates and elemental patterns. In the case of MRC-1, imaging shows intra-crystal zonation (Figs. 2 and 3), most apparent in the S map (though Sr, Nd, Th, and Ce maps also show variability to lesser extent; Fig. 3A). Apatite BRZ-1 does not display any apparent growth zones based on X-ray maps and CL images. Instead, imaging reveals chemical heterogeneity associated with wispy networks of micron-scale cracks that branch out over 5–20  $\mu m$  into the main matrix (Figs. 2 and 3). The X-ray maps indicate these cracks have similar Sr and Th contents compared to the unaltered matrix, but have lower S concentrations and higher Ce and Nd abundances (Fig. 3B).

To ensure comparability, electron microprobe analyses La, Ce, Nd, Pr, Si, Na, Th, Gd, Sm, Sr, Y, and S (Table 4) were measured along transects within the same areas used to develop X-ray maps. EPMA confirm a general decrease in measured trace element abundances from the interior to the exterior of the mapped MRC-1 grain. Aside from outliers associated with cracks or altered zones (discussed in detail in section 4.2.), BRZ-1 displays uniform elemental abundances across the grain (Fig. 3).

## 3.2. TIMS U-Pb, Sm-Nd, Sr

The primary MAD-UCSB apatite contains U-Pb compositions that are distinct from other previously reported Madagascar apatite ID-TIMS data (Thomson et al., 2012; Fisher et al., 2020b), differing in their degree of discordance (Fig. 4). MAD-UCSB apatite has an average U=22 ppm and average T=545 ppm (Table 6). The concordia age of MAD-UCSB as determined by the total Pb-U isochron method, which incorporates the measured  $^{204}$ Pb/ $^{206}$ Pb ratios (Schoene and Bowring, 2006; Ludwig, 2012), is  $467.4 \pm 8.4$  (9.8) Ma and yields a  $(^{207}$ Pb/ $^{206}$ Pb)<sub>i</sub> intercept of  $0.71 \pm 0.10$  (0.12) (n=6; MSWD = 0.2) (Fig. 4), similar to results from an unanchored York regression in a Tera-Wasserburg concordia diagram (isochron age of  $467 \pm 9$  Ma and a  $(^{207}$ Pb/ $^{206}$ Pb)<sub>i</sub> intercept of  $0.71 \pm 0.1$ ; MSWD = 0.003; all  $2\sigma$  analytical uncertainty).

MRC-1 apatite has average concentrations of U = 31 ppm and Th = 285 ppm, equivalent to a Th/U  $\approx 9$  (Table 6). All seven TIMS fractions define a single isochron (Fig. 5). The total Pb-U isochron method applied to these data yields an intercept age of 153.37  $\pm$  0.40 (0.42) Ma and a ( $^{207}\text{Pb}/^{206}\text{Pb})_i$  intercept of 0.85  $\pm$  0.04 (0.04) (MSWD = 1.9). The average U and Th concentrations of eight BRZ-1 ID-TIMS fractions are 65 ppm U and 892 ppm Th, or Th/U  $\approx$  14. The U-Pb data are highly dispersed (Fig. 5), but three fractions conform to a single population within an acceptable MSWD (Wendt and Carl, 1991). The total Pb-U isochron method for the these three fractions yields an intercept age of 2078  $\pm$  9 (12) Ma and a ( $^{207}\text{Pb}/^{206}\text{Pb})_i$  intercept of 1.14  $\pm$  0.07 (0.09) (MSWD = 0.2).

MAD-UCSB has  $^{143}\text{Nd}/^{144}\text{Nd}$  ratios that range between 0.511305  $\pm$  13 to 0.511342  $\pm$  10 (all present-day values), with an average  $^{143}\text{Nd}/^{144}\text{Nd}=0.511312\pm3$  (n = 6; MSWD = 8.2) or  $\epsilon_{\text{Nd}}=-25.7\pm0.11$  (values normalized to  $(^{143}\text{Nd}/^{144}\text{Nd})_{\text{CHUR}}=0.512630$ ; Bouvier et al., 2008). Corresponding  $^{147}\text{Sm}/^{144}\text{Nd}$  ratios span 0.07732  $\pm$  15 to

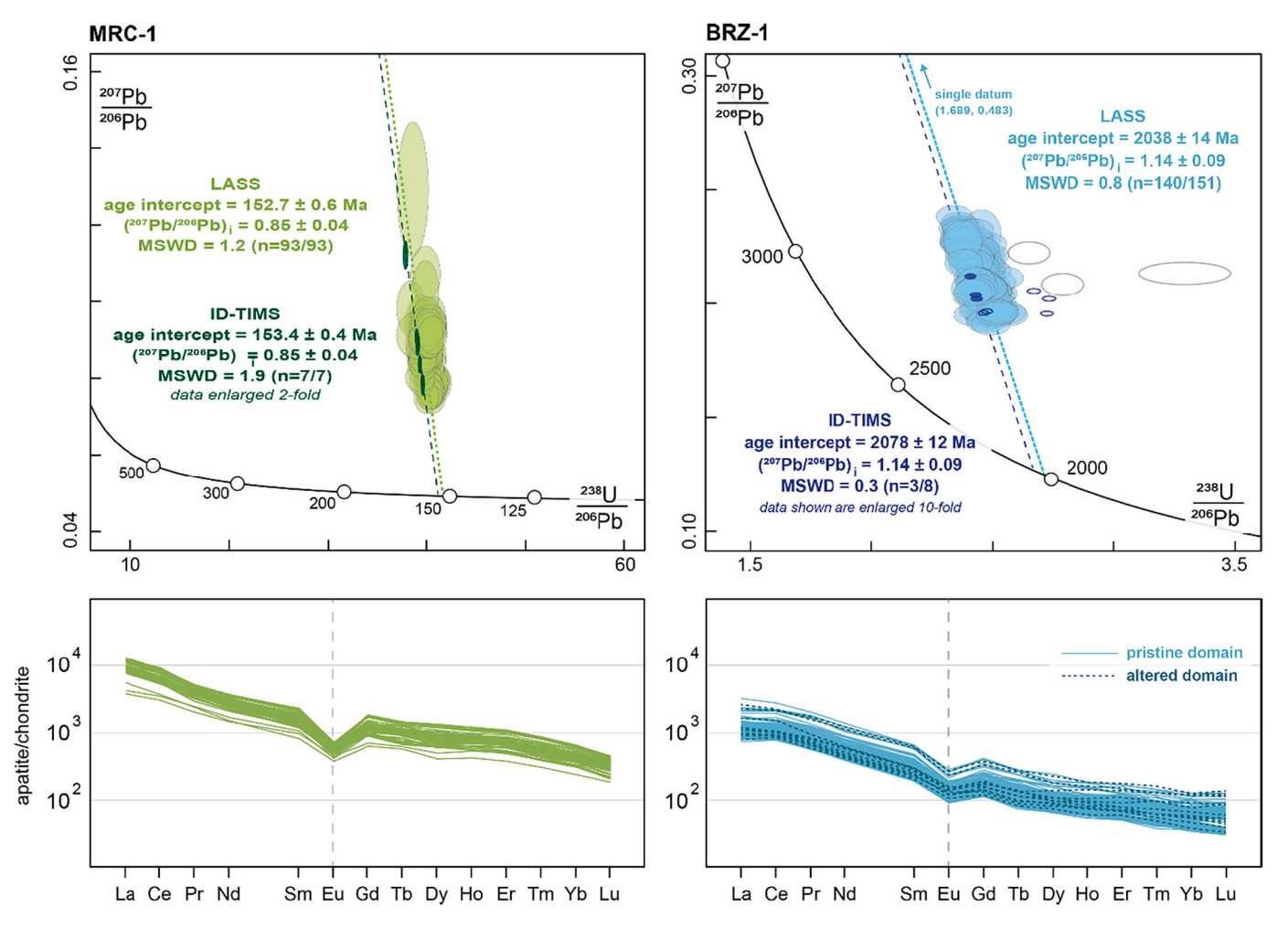


**Fig. 5.** Top: Tera-Wasserburg concordia diagrams of MRC-1 (right) and BRZ-1 (left) LASS data. The ages of the TIMS data were derived using the total Pb-U method, and the resulting ( $^{207}$ Pb/ $^{206}$ Pb)<sub>i</sub> intercepts were used to correct the LASS data. Unfilled ellipses are data excluded from age regression. Note that TIMS data are enlarged to facilitate visual comparison to the LASS data. TIMS and LASS analyses of MRC-1 produce overlapping isochrons, but produce offset isochrons for BRC-1. Bottom: Chondrite-normalized REE plots showing consistent REE patterns in these RMs (reference chondrite values from McDonough and Sun, 1995).

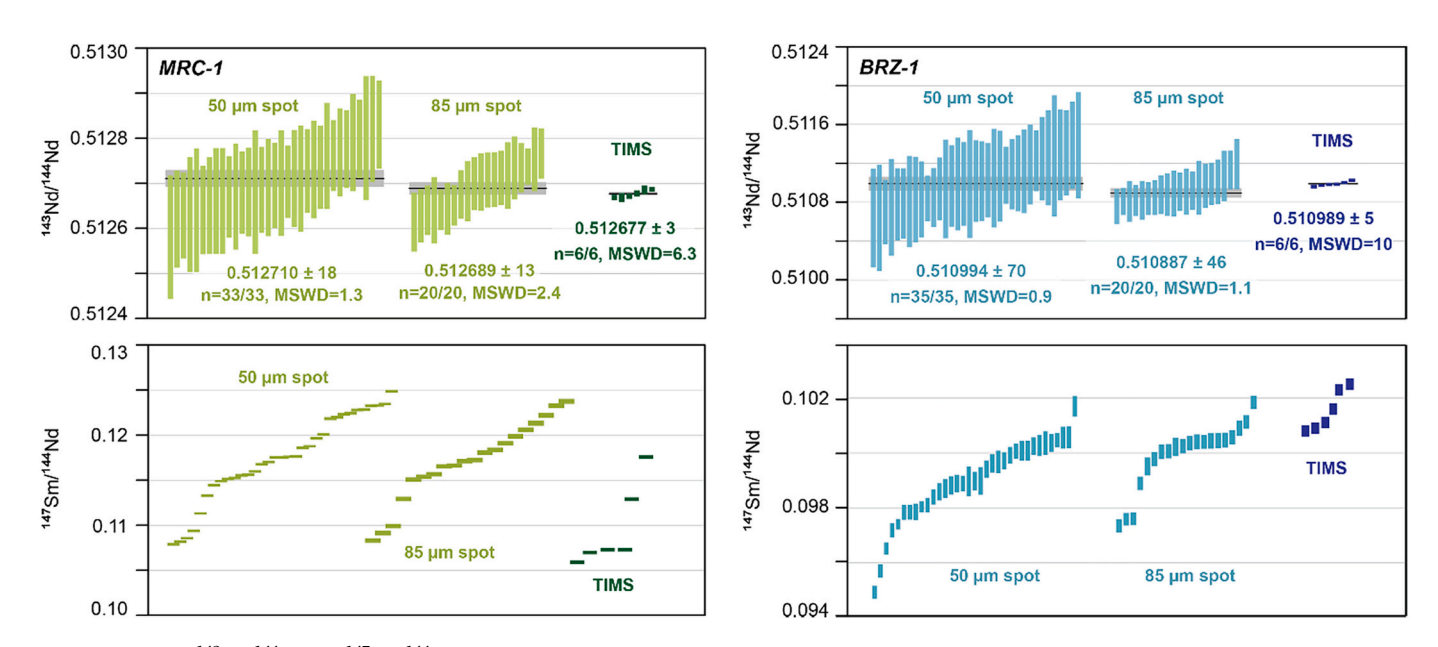


Fig. 6. Comparing  $^{143}$ Nd/ $^{144}$ Nd and  $^{147}$ Sm/ $^{144}$ Nd ratios obtained by LA-ICP-MS and ID-TIMS (same color scheme as Fig. 5). The height of each data point is the  $2\sigma$  uncertainty.

 $0.07787 \pm 16$  and produce an average  $^{147} Sm/^{144} Nd = 0.07763 \pm 4$  (Table 6). For MRC-1,  $^{143} Nd/^{144} Nd$  values cover a range from  $0.512668 \pm 10$  to  $0.512686 \pm 5$  (Fig. 6); the mean of the six measurements is  $0.512677 \pm 3$  (n = 6; MSWD = 6.3), or  $\epsilon_{Nd} = 0.9 \pm 0.1$ . The  $^{147} Sm/^{144} Nd$  ratios for MRC-1 are between  $0.10588 \pm 21$  and  $0.11755 \pm 24$ , with a mean  $^{147} Sm/^{144} Nd$  of  $0.10923 \pm 9$ . For BRZ-1, TIMS  $^{143} Nd/^{144} Nd$  ratios are between  $0.510961 \pm 15$  and  $0.511025 \pm 13$  with a weighted mean of  $0.510989 \pm 5$ , or  $\epsilon_{Nd} = -32.0 \pm 0.1$  (n = 6; MSWD = 10) (Fig. 6). The  $^{147} Sm/^{144} Nd$  values vary from  $0.10076 \pm 20$  to  $0.10247 \pm 20$ , with a mean  $^{147} Sm/^{144} Nd = 0.10152 \pm 8$  (Table 7).

The TIMS  $^{87}\text{Sr}/^{86}\text{Sr}$  ratios of MAD-UCSB are between  $0.711700\pm9$  and  $0.711798\pm8$  and produce a weighted mean  $^{87}\text{Sr}/^{86}\text{Sr}=0.711773\pm2$  (Table 8). The  $^{87}\text{Sr}/^{86}\text{Sr}$  ratios of MRC-1 range from  $0.707688\pm6$  to  $0.707695\pm5$  and yield a mean  $^{87}\text{Sr}/^{86}\text{Sr}=0.707691\pm2$  (MSWD =0.7) (Fig. 7). The BRZ-1  $^{87}\text{Sr}/^{86}\text{Sr}$  TIMS values range from  $0.709136\pm11$  to  $0.709231\pm8$  and result in a mean  $^{87}\text{Sr}/^{86}\text{Sr}$  ratio of  $0.709188\pm3$  (MSWD =134) (Fig. 7). Although the weighted mean  $^{87}\text{Sr}/^{86}\text{Sr}$  value for BRZ-1 does not represent statistically single population, we note that variability at this scale cannot be readily distinguished by LA-ICP-MS (see section 3.4.).

#### 3.3. LASS U-Pb and trace elements

A total of 93 LASS spots collected across MRC-1—including a c-axis perpendicular section—comport to an isochron and overlap the seven ID-TIMS fractions (Fig. 5). Laser ablation spot analyses corroborate elemental variability within MRC-1 (Fig. 8), however, all spots show

**Table 8**Summary of Sr results from this study.

Apatite	Method	Average Sr [ppm]	$^{87}$ Sr/ $^{86}$ Sr $^{a}$	Offset <sup>b</sup>
	ID-TIMS	1847	$\textbf{0.711773} \pm \textbf{2}$	-
MAD- UCSB	LA-ICP-MS (50 μm)	1577	$0.711850 \pm 120$	-0.02
OCSD	LA-ICP-MS (85 μm)	1567	$0.712028 \pm 86$	-0.04
	ID-TIMS	779	$0.707691 \pm 2$	-
MRC-1	LA-ICP-MS (50 μm)	700	$0.708092 \pm 180$	-0.06
	LA-ICP-MS (85 μm)	695	$0.708325 \pm 80$	-0.09
	ID-TIMS	233	$\textbf{0.709188} \pm 3$	-
BRZ-1	LA-ICP-MS (50 μm)	243	$0.710550 \pm 560$	-0.19
	LA-ICP-MS (85 μm)	246	$0.710768 \pm 178$	-0.22
Dunonoo	LA-ICP-MS (50 μm)	335	$0.708380 \pm 510$	-0.30
Durango	LA-ICP-MS (85 μm)	335	$0.709030 \pm 190$	-0.39
McClure	LA-ICP-MS (50 μm)	3155	$0.703655 \pm 74$	0.00
McGlure	LA-ICP-MS (85 μm)	2882	$0.703778 \pm 28$	-0.01
401	LA-ICP-MS (50 μm)	383	$0.707220 \pm 490$	-
401	LA-ICP-MS (85 μm)	392	$0.707180 \pm 150$	-
OD306	LA-ICP-MS (50 μm)	142	$\begin{array}{c} \textbf{0.711200} \ \pm \\ \textbf{1700} \end{array}$	-
OD300	LA-ICP-MS (85 μm)	137	$0.710890 \pm 450$	-
DINIO	LA-ICP-MS (50 μm)	184	$0.703090 \pm 940$	0.05
BHVO	LA-ICP-MS (85 μm)	198	$0.703440 \pm 330$	0.00
MACS-3	LA-ICP-MS (25 μm)	-	$0.707390 \pm 140$	0.02

<sup>&</sup>lt;sup>a</sup> Weighted mean and associated 2σ uncertainty; unnormalized.

similar REE patterns: they are LREE-enriched (La/Yb<sub>N</sub>  $\approx$  20–30) and display a negative Eu anomaly (Eu/Eu\*  $\approx$  0.4, where Eu/Eu\*= $\frac{Eu_N}{\sqrt{Sm_N \times Gd_N}}$ ) (Fig. 5).

Most LASS spots collected from the BRZ-1 apatite (n=188/196) fall along a well-defined isochron, including those measured perpendicular to the c-axis (Fig. 5). Some data fall off this isochron and project to dates as young as ca. 865 Ma. Notably, LASS spots document that HREEs and U are enriched in younger domains associated with these cracks (Figs. 8 and 9). Portions of BRZ-1 away from cracks are LREE-enriched (La/Yb\_N  $\approx 20$ –28) and have a negative Eu anomaly (Eu/Eu\*  $\approx 0.6$ –0.8) (Fig. 5).

#### 3.4. LA-ICP-MS Sm-Nd and Sr isotopes

Thirty-three 50-µm-diameter spots across MRC-1 overlap the ID-TIMS values and yield a weighted mean  $^{143}$ Nd/ $^{144}$ Nd of 0.512710  $\pm$ 18 ( $\varepsilon_{Nd} = 1.4 \pm 0.4$ ; MSWD = 1.3), which are slightly higher than the TIMS mean (Table 7; Fig. 6). The corresponding 147Sm/144Nd values vary from 0.1078  $\pm$  1 to 0.1247  $\pm$  2, which partially overlap the TIMS  $^{147}$ Sm/ $^{144}$ Nd range but are typically higher (Fig. 6). Twenty 85 µm-wide spots yield  $^{143}$ Nd/ $^{144}$ Nd values produce a weighted mean of 0.512689  $\pm$ 13 ( $\epsilon_{Nd} = 1.0 \pm 0.3$ ; MSWD = 2.4); this value is indistinguishable within  $2\sigma$  uncertainty from the mean of the 50- $\mu$ m-diameter spots and TIMS data. The <sup>147</sup>Sm/<sup>144</sup>Nd values determined using an 85-μm-diameter spot vary from 0.1171  $\pm$  3 to 0.1237  $\pm$  3, which like the 50- $\mu$ m spots, tend to be on the higher end of TIMS <sup>147</sup>Sm/<sup>144</sup>Nd range (Fig. 6). Laser ablation data for BRZ-1 with a 50-µm-diameter spot produce <sup>143</sup>Nd/<sup>144</sup>Nd values that overlap the TIMS range and yield a weighted mean <sup>143</sup>Nd/<sup>144</sup>Nd =  $0.510994 \pm 70 \ (\epsilon_{Nd} = -32.1 \pm 1.4; MSWD = 0.9, n = 35); ^{147} Sm/^{144} Nd$ values vary from 0.0949  $\pm$  2 to 0.1017  $\pm$  4, which generally fall within the TIMS <sup>147</sup>Sm/<sup>144</sup>Nd range (Table 7; Fig. 6). Analyses utilizing an 85- $\mu$ m-diameter spot result in a mean  $^{143}$ Nd/ $^{144}$ Nd = 0.510887  $\pm$  46 ( $\epsilon$ Nd)  $= -34.2 \pm 0.9$ ; MSWD = 1.1, n = 20) (Fig. 6). While the mean of the 85 um spots are offset from the TIMS mean, the ranges of the LA data are wholly consistent with the TIMS data (Fig. 6). The <sup>147</sup>Sm/<sup>144</sup>Nd values have a range between  $0.0973 \pm 2$  and  $0.1018 \pm 2$ , which largely overlap the TIMS <sup>147</sup>Sm/<sup>144</sup>Nd values but do not extend to as high values

Despite corrections for Kr, REEs, Ca-dimer, and Rb interferences,  $^{87}\mathrm{Sr}/^{86}\mathrm{Sr}$  measurements collected by LA-ICP-MS were persistently offset from TIMS reference values (Fig. 7). For MRC-1, the average corrected  $^{87}\text{Sr}/^{86}\text{Sr}$  value of the 50 µm spot analyses is 0.70809  $\pm$  18 (MSWD =1.3, n = 10), which is ~0.05% higher than its TIMS average (Table 8; Fig. 7). The average <sup>87</sup>Sr/<sup>86</sup>Sr value collected using an 85-µm-diameter spot is  $\sim$ 0.08% higher than the TIMS average ( $^{87}$ Sr/ $^{86}$ Sr = 0.708325  $\pm$ 80, MSWD = 2.3, n = 15). Offsets between LA and TIMS averages of BRZ-1 are more dramatic. The <sup>87</sup>Sr/<sup>86</sup>Sr average determined using a 50- $\mu$ m-diameter spot are  $^{87}$ Sr/ $^{86}$ Sr = 0.71055  $\pm$  56 (~0.19% higher than TIMS); using an 85- $\mu$ m-diameter spot produces an average  $^{87}$ Sr/ $^{86}$ Sr =  $0.710768 \pm 178$  (  $\sim\!0.22\%$  higher than TIMS; Fig. 7). The other analyzed RMs are also offset from the TIMS reference value, and are anticorrelated with the inverse of the measured <sup>88</sup>Sr signal (Fig. 10). Normalization to a primary RM (e.g., MAD-UCSB) does not remove this trend, but only shifts the averages towards more radiogenic values. Though <sup>87</sup>Rb/<sup>86</sup>Sr ratios were not analyzed by TIMS, and hence their accuracy is unknown, in situ <sup>87</sup>Rb/<sup>86</sup>Sr ratios are low (<0.0002), indicating that radiogenic ingrowth of <sup>87</sup>Sr is negligible.

# 4. Discussion

# 4.1. Common-Pb corrections and U-Pb ages

Apatite incorporates significant amounts of non-radiogenic (common) Pb as it crystallizes, necessitating corrections to obtain geologically meaningful U-Pb dates. Common-Pb corrections can be done using different methods: from unanchored linear regression through multiple

 $<sup>^{\</sup>rm b}$  Defined as 100  $\times$  [1 - ( $^{87}{\rm Sr}/^{86}{\rm Sr})_{\rm LA}$  / ( $^{87}{\rm Sr}/^{86}{\rm Sr})_{\rm TIMS}$ ].

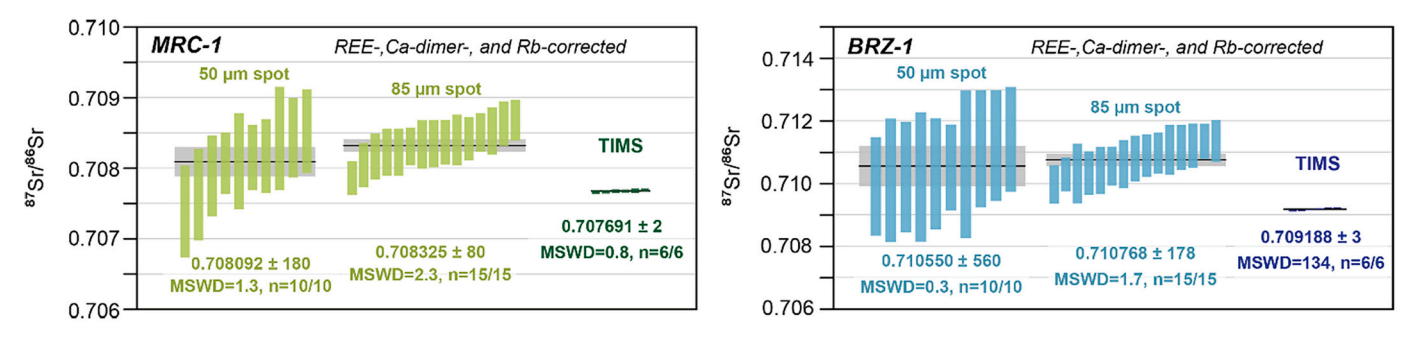


Fig. 7. Comparing  $^{87}$ Sry $^{86}$ Sr values obtained by LA-ICP-MS and ID-TIMS (same color scheme as Fig. 5). Laser ablation data are REE-, Ca-dimer, and Rb-corrected, and not normalized to a primary RM. Note that while laser ablation Sr values determined using 50 and 85  $\mu$ m overlap on another, they are persistently offset from TIMS values. The height of each data point is the  $2\sigma$  uncertainty.

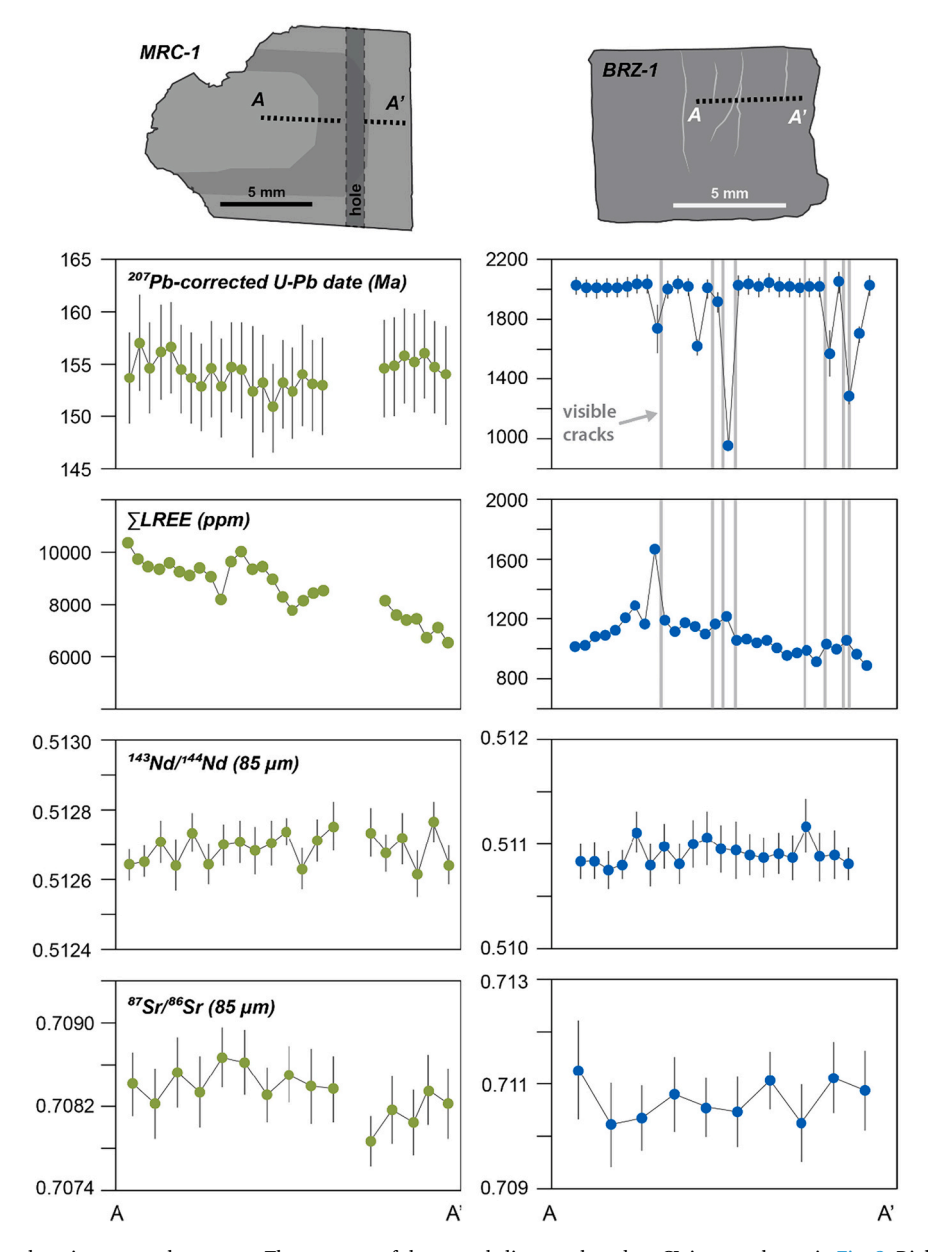
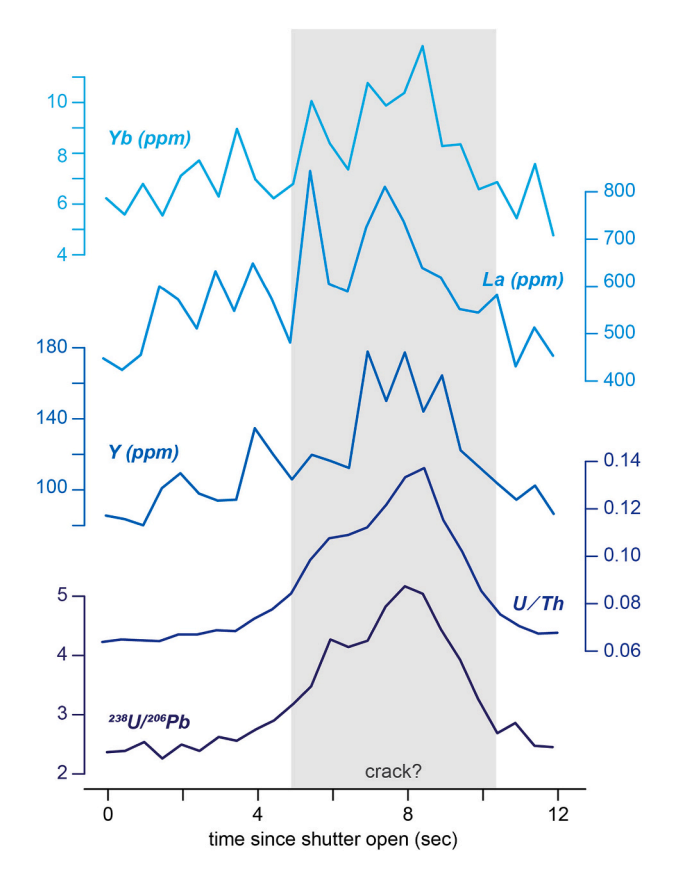


Fig. 8. Assessing variability along intra-crystal transects. The cartoons of the crystal slices are based on CL images shown in Fig. 2. Right: MRC-1 data. Left: BRZ-1 data. All transects projected onto the A-A' line. Uncertainties shown are  $2\sigma$ . Total LREE is the sum of La, Ce, Pm, and Nd abundances. Note that U-Pb and LREE spikes in BRZ-1 are spatially associated with cracks in the crystal.



**Fig. 9.** Time-resolved laser ablation split stream profile for a BRZ-1 spot analysis. U-Pb ratios spike at depth, coincident with increases in U/Th, Y, La, and Yb. These spikes indicate the presence of a chemically-distinct domain within the apatite (probably a crack; see Fig. 3). Spot analyses like this deviate from the 2.0 Ga isochron shown in Fig. 5.

data points that form isochrons, using the total Pb-U isochron method that incorporates <sup>204</sup>Pb measurements (see section 2.5.), by implementing the Pb growth model of Stacey and Kramers (1975), or by analyzing Pb isotopes in co-genetic, low U/Pb phases (e.g., feldspar; Chamberlain and Bowring, 2001; Schoene and Bowring, 2006; Chew et al., 2014a). The latter is not applicable here because the analyzed apatites were obtained as individual crystals. In addition, because <sup>204</sup>Pb cannot always be accurately measured by LA-ICP-MS given isobaric interferences with <sup>204</sup>Hg present in the He carrier gas and Ar plasma gas, the total Pb-U approach cannot be readily applied to our laser ablation data

Applying different common-Pb correction schemes has no significant effect on the calculated intercept ages of the RMs (Table 6). In the case of MRC-1, the concordia age derived from the total Pb-U method applied to the TIMS data is 153.4  $\pm$  0.4, which is indistinguishable from an unanchored York regression in Tera-Wasserburg concordia space (153.5  $\pm$ 0.4 Ma) and an anchored regression to a Stacey and Kramers (1975) model ( $^{207}\text{Pb}/^{206}\text{Pb}$ ); (153.4  $\pm$  0.4 Ma; Table 6). The LASS data yield comparable concordia ages of 152.7  $\pm$  0.6 Ma for data anchored to the (<sup>207</sup>Pb/<sup>206</sup>Pb)<sub>i</sub> value derived from the total Pb-U method of the TIMS data and 152.8  $\pm$  0.9 Ma using the Stacey and Kramers (1975) model; unanchored regressions through the LASS data are not possible. For the three data that conform to a single population in BRZ-1 TIMS data set, the total Pb-U method yields a concordia age of 2078  $\pm$  12 Ma, which overlaps within uncertainty age intercepts derived from unanchored regressions (2077  $\pm$  14 Ma) and a Stacey and Kramers (1975) common-Pb model (2069  $\pm$  11 Ma). The LASS data for BRZ-1 produce consistent U-Pb ages. Applying the (<sup>207</sup>Pb/<sup>206</sup>Pb)<sub>i</sub> value derived from the total Pb-U method of the TIMS data yields 2038  $\pm$  14 Ma; this age overlaps the unanchored isochron age of 2042  $\pm$  12 Ma and Stacey and Kramers (1975) anchored age of 2038  $\pm$  11 Ma (Table 6). Regardless of the chosen (207Pb/206Pb)<sub>i</sub>, the LASS and TIMS BRZ-1 ages are offset beyond their respective internal  $2\sigma$  uncertainties (Fig. 6). This deviation is likely to reflect minor incorporation of younger, reset age domains during LASS spot analyses, as discussed below.

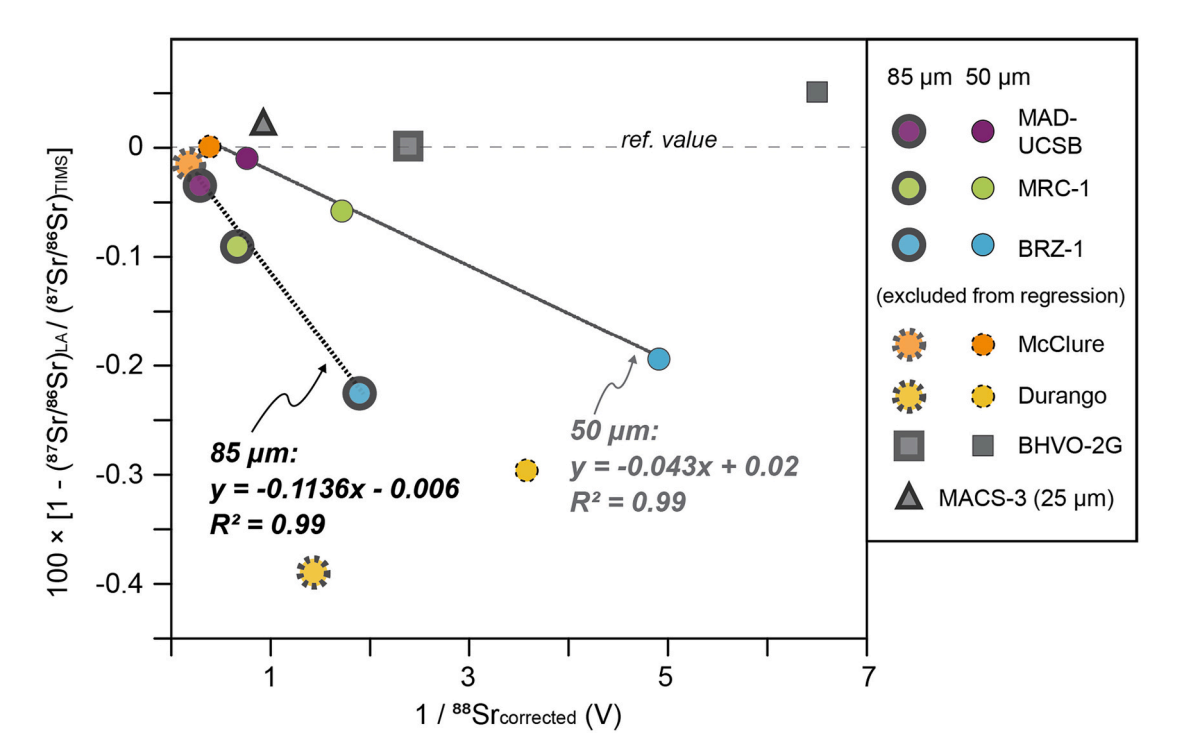


Fig. 10. Offset between average  $^{87}$ Sr/ $^{86}$ Sr ratios determined by LA-ICP-MS and ID-TIMS vs. inverse of interference-corrected  $^{88}$ Sr signal intensity. Data for RMs from this study define a linear anti-correlation trend that could be used to empirically correct  $^{87}$ Sr/ $^{86}$ Sr. Typical 2σ uncertainties are smaller than the size of each symbol. Linear fits do not consider the uncertainty of individual datum.

#### 4.2. Fluid-assisted U-Pb resetting in BRZ-1 apatite

Although the choice of common-Pb composition does not significantly affect the age intercepts of the individual BRZ-1 ID-TIMS and LASS data sets, there is a persistent ~1.6% difference in the mean ages (Fig. 5). This difference is unlikely to reflect matrix effects (e.g., Gehrels et al., 2008; Sylvester, 2008; Thompson et al., 2016) because there are no significant correlations among age offset vs. elemental compositions of the RMs (Supplementary Fig. S1). The age differences for BRZ-1 also cannot simply be a result of U-Pb heterogeneity in the primary MAD-UCSB reference apatite because all other secondary RMs (including MRC-1) are within uncertainty of their established ages, and shifting the U-Pb composition of MAD-UCSB to bring the BRZ-1 TIMS and LASS dates to parity would cause offsets in these other RMs.

Overprinting or partial Pb loss is the likely root cause of the age shifts BRZ-1 data sets. It is clear from CL imaging and elemental X-ray maps that compositional heterogeneity is closely associated with cracks (Fig. 3B). Generally, LASS spots overlapping/near these cracks deviate the most from the ca. 2.07 Ga isochron, but it is also apparent that relatively young dates occur in the absence of any obvious cracks in a few cases (Fig. 8). In these cases, we suspect that some portion of the LASS spot analyses intersected cracks at depth, skewing the isochron towards a younger intercept age (Fig. 9). Minor amounts of the altered domains are likely incorporated into most of the LASS analyses given that heterogeneity occurs at a scale that is beyond the typical precision of LASS. The TIMS analyses highlight the fine-scale at which heterogeneity occurs. Three TIMS fractions from BRZ-1 form a coherent population, two other points lie slightly off the 2.07 Ga isochron, and three are clearly situated away with the isochron (Fig. 5); the uncertainty of individual LASS analyses is unable to resolve minor amounts of mixing with the younger domains (i.e., the two slightly discordant TIMS fractions) and helps explain why the LASS analyses yield an apparently younger intercept age.

Evidence for fluid-mediated isotopic resetting in BRZ-1 apatite is observed as µm-scale fractures with distinct elemental compositions (Fig. 2C). Both EPMA and LASS spot analyses reveal that altered domains are characterized by elevated REE and Th concentrations relative to the unaltered matrix. The exact nature of the fluid is uncertain but reactions with aqueous fluids would be expected to deplete REEs in apatite (e.g., Harlov et al., 2005), which is contrary to the observed increase in REE concentrations associated with cracks (Fig. 9). Experiments exploring REE partitioning between apatite and silicate melt indicate that REEs are compatible in apatite over melts (Prowatke and Klemme, 2006), but it is unclear how such viscous fluids would infiltrate through the fine-grained cracks. Rigorous testing of fluid compositions would require further petrological context, but regardless of the exact nature of the metasomatic agent, it is clear that monitoring and screening of BRZ-1 analyses are required if it is to be employed as an effective RM.

Coupled U-Pb and trace-element data can be useful in screening altered domains in BRZ-1. Fig. 9 shows that highly discordant spot analyses correlated with higher concentrations of some trace elements, including U and REEs, in agreement with findings from EPMA (Fig. 3). Unfortunately, these trends are apparent for spot analyses showing extreme discordance; trace elements are unable to discriminate minor degrees of mixing with younger age domains in BRZ-1 (Fig. 5). Another way to optimize this apatite for petrochronology would be to preferentially break the apatite along altered cracks and remove the exterior of different crystal fragments either by hand-polishing or air abrasion, ensuring only pristine areas are targeted.

# 4.3. Limitations of in situ Sr isotopic analyses and ways forward

In situ Sr isotope analyses of the apatite RMs can differ from TIMS reference values by up to 0.02% (Fig. 10). While there are multiple unresolved interferences in our study that could account for these

offsets—like Hf, MnP, and Fe-oxides, which both occur as trace elements within apatite (Ramos et al., 2004; Gillespie et al., 2021b)-a critical interference is likely to be <sup>40</sup>Ca<sup>31</sup>P<sup>16</sup>O<sup>+</sup> (CaPO), a molecule formed of major elements within apatite. Indeed, Horstwood et al. (2008) observed a similar deviation trend, wherein apatite with lower Sr concentrations are more offset towards radiogenic values than those with higher Sr contents. Horstwood et al. suggested that CaPO can contribute significantly to the <sup>87</sup>Sr signal (up to 1%) and that <sup>87</sup>Sr/<sup>86</sup>Sr compositions by LA-ICP-MS are likely only accurate to 0.03-0.4% without correcting for this interference. Hence, apatite with lower Sr concentrations is expected to yield greater differences given the relatively greater contribution of CaPO on <sup>87</sup>Sr. Unfortunately, monitoring the contributions of CaPO on the <sup>87</sup>Sr signal requires measurement of mass-71 (corresponding to <sup>40</sup>Ca<sup>31</sup>P) and precise knowledge of oxide production during an analytical session, information we are unable to obtain with the MC-ICP-MS set-up used in this study. There is also the likelihood that LREE-oxides create some interferences on middle REEs used to correct isobaric interferences with Sr (e.g., Kent and Ungerer, 2005). Despite these complexities, we suggest that calibrations against multiple apatite RMs provide an alternative way to obtain accurate <sup>87</sup>Sr/<sup>86</sup>Sr measurements by LA-ICP-MS.

Analyses of apatite whose TIMS Sr isotopic compositions have been determined for the purpose of this study (MAD-UCSB, BRZ-1, and MRC-1) define a strong anti-correlation between <sup>87</sup>Sr/<sup>86</sup>Sr offset—defined here as  $100 \times [1 - (^{87}\text{Sr}/^{86}\text{Sr})_{LA} / (^{87}\text{Sr}/^{86}\text{Sr})_{TIMS}]$ —and  $1/^{88}\text{Sr}_{corrected}$ signal intensity ( $R^2 = 0.99$  for analyses using 50- and 85-µm-diameter laser spots; Fig. 10). This empirical trend could be used to correct in situ Sr isotopic measurements. We find that McClure apatite is also situated along this empirical trend, but our Sr analyses of Durango are not (Fig. 10). This could signify that the effects of CaPO and other interferences are non-linear or that different Durango crystals have distinct intracrystal <sup>87</sup>Sr/<sup>86</sup>Sr compositions. Multiple ID-TIMS analyses of different Durango crystals are consistent with one another (McFarlane and McCulloch, 2008; Horstwood et al., 2008; Hou et al., 2013; Yang et al., 2014; Table 3), suggesting yet another unresolved interference hampers in situ <sup>87</sup>Sr/<sup>86</sup>Sr measurements. One distinguishing aspect of Durango apatite is its high Cl proportion (~0.4 wt%) relative to other apatite RMs: MAD (~0.2 wt% Cl) and McClure (~0.02 wt% Cl) (Chew et al., 2014b; Yang et al., 2014). As a result, there may be an interference on  $^{87}\text{Sr}$  from  $^{40}\text{Ca}^{37}\text{Cl}$  in Durango that causes a larger offset from <sup>87</sup>Sr/<sup>86</sup>Sr TIMS reference values compared to other apatite with lower Cl concentrations. Future studies should therefore consider Cl concentrations when deciding the most appropriate RMs for in situ <sup>87</sup>Sr/<sup>86</sup>Sr measurements.

Although the Sr isotopic compositions of 401 and OD306 apatites (Thompson et al., 2016) have not been previously analyzed, we can estimate their  $^{87}\text{Sr}/^{86}\text{Sr}$  compositions based on our observed empirical trend and average measured  $^{88}\text{Sr}$  intensities. For 401 apatite, corrected  $^{87}\text{Sr}/^{86}\text{Sr}$  values are  $0.706406\pm489$  (50  $\mu m$  spot) and  $0.706180\pm150$  (85  $\mu m$  spot). For OD306, corrected  $^{87}\text{Sr}/^{86}\text{Sr}$  values are  $0.708741\pm1694$  (50  $\mu m$  spot) and  $0.708015\pm448$  (85  $\mu m$  spot) (note that these the corrected  $^{87}\text{Sr}/^{86}\text{Sr}$  values do not include errors of the fits). Large uncertainties notwithstanding, the corrected Sr value for OD306 should be accurate giving that Cl concentrations are relatively low ( $\sim\!0.1$  wt% Cl; Thompson et al., 2016), whereas 401 could be considerably more inaccurate ( $\sim\!0.7$  wt% Cl; Thompson et al., 2016).

Finally, the Sr isotopic compositions of silicate glass BHVO-2G and carbonate MACS-3 determined by LA-ICP-MS in this study are consistently more accurate than our apatite analyses at similar Sr concentrations (typically within 2σ uncertainty of their preferred GeoReM TIMS <sup>87</sup>Sr/<sup>86</sup>Sr compositions; Table 3; Fig. 10). Both BHVO-2G and MACS-3 are characterized by significantly lower Ca, P, and REEs contents for similar Sr concentrations compared the apatite RMs (Table 3). These observations support the interpretation that CaPO interferences, among other interferences, may be significant hindrances in obtaining accurate in situ <sup>87</sup>Sr/<sup>86</sup>Sr in apatite. In total, our study strongly suggests that

analyzing a suite of matrix-matched RMs with well-characterized <sup>87</sup>Sr/<sup>86</sup>Sr isotopic values and different Sr concentrations are critical for corrections and obtaining robust measurements by LA-ICP-MS.

#### 4.4. Recommended reference values

Reference values for MRC-1 and BRZ-1 are available in the Supplementary Materials in a format that can be readily transferred to a Standard file for Iolite. For reference apatites with variable amounts of common-Pb, the common-Pb and concordia age intercepts—rather than individual or average U/Pb ratios—are key parameters for calibrating and assessing accuracy of U-Pb analyses (Petrus and Kamber, 2012; Chew et al., 2014a). As discussed above, common-Pb compositions and concordia ages are robust: initial Pb compositions determined by the total Pb-U method and by unanchored regressions are within 2<sub>\sigma</sub> uncertainty of each other and the Stacey and Kramers (1975) model compositions, and concordia age intercepts are insensitive to the choice of common-Pb (Table 6). The recommended concordia ages and common-Pb compositions are derived from the total Pb-U method applied to the ID-TIMS analyses and incorporate the internal error and tracer uncertainties (0.03% for <sup>238</sup>U/<sup>206</sup>Pb; see section 2.3). The recommended Sm-Nd and Sr isotopic values are also established by TIMS analyses and incorporate internal error and tracer uncertainties (see sections 2.4). The reported values are the weighted means of the data, with the caveat the associated MSWDs can be large. Variability at this scale is, however, beyond typically  $2\sigma$  uncertainties for LA-ICP-MS (Figs. 6 and 7) and are therefore appropriate as reference values for in situ analyses.

Reference elemental values reported in Supplementary Tables S1 and S2 are based on a mixture of EPMA and LASS data. We utilize the EPMA elemental data where it exists and LASS data for the others. Like the corresponding U-Pb data, the apatite RMs can be heterogeneous across the crystal with respect to elemental concentrations (Fig. 8). For BRZ-1, we excluded data based on corresponding U-Pb dates that exhibit extreme discordance from the reported averages (Fig. 9).

#### 5. Conclusions

Two prospective reference apatites from Morocco (MRC-1) and Brazil (BRZ-1) provide new tools for in situ apatite analyses. The MRC-1 apatite, despite being compositionally zoned, yields consistent U-Pb concordia dates (Fig. 5). The U-Pb compositions of MRC-1 vary along a well-defined isochron and can be employed as a primary standard using, for example, the VizualAge UcomPbine data reduction scheme for Iolite (Chew et al., 2014a), which can correct for variable amounts of common-Pb in different RMs. The Nd isotopic compositions determined by LA-ICP-MS for MRC-1 are consistent and comparable to those obtained by ID-TIMS, making it most useful as a <sup>143</sup>Nd/<sup>144</sup>Nd isotopic RM. The ID-TIMS <sup>87</sup>Sr/<sup>86</sup>Sr compositions for MRC-1 are remarkably homogeneous (Fig. 7) and is a strong candidate for a Sr RM; we emphasize the need for such an RM given the challenges of obtaining precise and accurate Sr compositions by LA-ICP-MS and SIMS in the face of confounding isobaric interferences (Gillespie et al., 2021b).

The data discussed above indicate that the BRZ-1 apatite is best utilized as a secondary standard. Its U concentrations are conducive for relatively precise dating (Table 6), and the vast majority of the matrix yields U-Pb data that fall along a single ca. 2.07 Ga isochron (Fig. 5). Heterogeneity in these crystals occurs as micron-scale cracks associated with secondary-alteration, which is a disadvantage of this RM. Imaging (either by BSE or CL) would be useful in guiding spot placement to ensure only pristine portions of the grain are targeted. Combined trace element analyses are useful for identifying U-Pb data that have been partially reset and emphasize the advantage of LASS in interpreting complex age patterns in apatite. The LA-ICP-MS Nd isotopic measurements of BRZ-1 are homogeneous within typical 2σ uncertainties (Fig. 7), agree well with the mean Nd isotopic compositions determined

by TIMS, and appear largely unaffected by micron-scale heterogeneity within our reported LA-ICP-MS  $2\sigma$  uncertainties. Concentrations of Sr are low in BRZ-1 (average  $\sim 200{-}300$  ppm), requiring large spot sizes (>85  $\mu m$  diameter) to obtain precise Sr isotopic measurements by LA-ICP-MS. However, BRZ-1 provides a useful anchor for empirical calibrations of deviation trends in  $^{87}\text{Sr}/^{86}\text{Sr}$  measurements by LA-ICP-MS and SIMS.

Finally, we are offering to send individual slices of MRC and BRZ apatite crystals to interested parties, and ask that data collected from these RMs be returned to us so that we may compare laboratory results. As is the case for all natural RMs, only limited material from the exact crystals investigated in this study exist. While we have procured and are willing to distribute other MRC and BRZ crystals, we cannot guarantee that their isotopic or elemental compositions are identical to the ones reported here. We therefore encourage additional ID-TIMS analyses to verify the compositions of other MRC and BRZ apatite crystals.

Supplementary data to this article can be found online at https://doi.org/10.1016/j.chemgeo.2021.120689.

#### **Declaration of Competing Interest**

The authors declare that they have no known competing financial interests or personal relationships that could have appeared to influence the work reported in this paper.

#### Acknowledgements

Funding was provided by the AGeS2 program via National Science Foundation (NSF) grants EAR-1759200 and EAR-1759353, as well as NSF grant EAR-1650260 to R Rudnick and J Cottle and an NSF graduate research fellowship to F Apen. We thank Christopher Fisher for sharing the Iolite Sm-Nd data reduction scheme and the common-Pb uncorrected MAD2-TCD data, and Roberta Rudnick for comments on an early version of the manuscript. Thoughtful and constructive reviews from David Chew and Anonymous are greatly appreciated, as is the efficient editorial handling of Catherine Chauvel. Those interested in obtaining pieces of the apatite RMs should contact the first author (while supplies last). Any opinions, findings, and conclusions or recommendations expressed in this material are those of the authors and do not necessarily reflect the views of the NSF.

#### References

- Amelin, Y., Zaitsev, A.N., 2002. Precise geochronology of phoscorites and carbonatites: the critical role of U-series disequilibrium in age interpretations. Geochim. Cosmochim. Acta 66, 2399–2419. https://doi.org/10.1016/S0016-7037(02)00831-1.
- Antoine, C., Bruand, E., Guitreau, M., Devidal, J.-L., 2020. Understanding preservation of primary signatures in apatite by comparing matrix and zircon-hosted crystals from the Eoarchean Acasta Gneiss Complex (Canada). Geochem. Geophys. Geosyst. 21. https://doi.org/10.1029/2020GC008923
- Apen, F.E., Rudnick, R.L., Cottle, J.M., Kylander-Clark, A.R.C., Blondes, M.S., Piccoli, P. M., Seward, G., 2020. Four-dimensional thermal evolution of the East African Orogen: accessory phase petrochronology of crustal profiles through the Tanzanian Craton and Mozambique Belt, northeastern Tanzania. Contrib. Mineral. Petrol. 175, 97. https://doi.org/10.1007/s00410-020-01737-6.
- Barfod, G.H., Krogstad, E.J., Frei, R., Albarède, F., 2005. Lu-Hf and PbSL geochronology of apatites from Proterozoic terranes: a first look at Lu-Hf isotopic closure in metamorphic apatite. Geochim. Cosmochim. Acta 69, 1847–1859. https://doi.org/ 10.1016/j.gca.2004.09.014.
- Belousova, E.A., Griffin, W.L., O'Reilly, S.Y., Fisher, N.I., 2002. Apatite as an indicator mineral for mineral exploration: trace-element compositions and their relationship to host rock type. J. Geochem. Explor. 76, 45–69. https://doi.org/10.1016/S0375-6742(02)00204-2.
- Bizzarro, M., Simonetti, A., Stevenson, R.K., Kurszlaukis, S., 2003. In situ 87Sr/86Sr investigation of igneous apatites and carbonates using laser-ablation MC-ICP-MS. Geochim. Cosmochim. Acta 67, 289–302. https://doi.org/10.1016/S0016-7037(02) 01048-7
- Bouvier, A., Vervoort, J.D., Patchett, P.J., 2008. The Lu-Hf and Sm-Nd isotopic composition of CHUR: Constraints from unequilibrated chondrites and implications for the bulk composition of terrestrial planets. Earth Planet. Sci. Lett. 273, 48–57. https://doi.org/10.1016/j.epsl.2008.06.010.

Bruand, E., Fowler, M., Storey, C., Darling, J., 2017. Apatite trace element and isotope applications to petrogenesis and provenance. Am. Mineral. 102, 75–84. https://doi. org/10.2138/am-2017-5744.

- Bruand, E., Fowler, M., Storey, C., Laurent, O., Antoine, C., Guitreau, M., Heilimo, E., Nebel, O., 2020. Accessory mineral constraints on crustal evolution: elemental fingerprints for magma discrimination. Geochemical Perspect. Lett. 13, 7–12. https://doi.org/10.7185/geochemlet.2006.
- Carrapa, B., DeCelles, P.G., Reiners, P.W., Gehrels, G.E., Sudo, M., 2009. Apatite triple dating and white mica 40Ar/39Ar thermochronology of syntectonic detritus in the Central Andes: a multiphase tectonothermal history. Geology 37, 407–410. https:// doi.org/10.1130/G25698A.1.
- Catanzaro, E.J., Murphy, T.J., Shields, W.R., Garner, E.L., 1968. Absolute isotopic abundance ratios of common, equal-atom, and radiogenic lead isotopic standards. J. Res. Natl. Bur. Stand. Sect. A Phys. Chem. 72A, 261. https://doi.org/10.6028/ ires.072A.025.
- Chamberlain, K.R., Bowring, S.A., 2001. Apatite–feldspar U–Pb thermochronometer: a reliable, mid-range (~450°C), diffusion-controlled system. Chem. Geol. 172, 173–200. https://doi.org/10.1016/S0009-2541(00)00242-4.
- Chew, D.M., Sylvester, P.J., Tubrett, M.N., 2011. U–Pb and Th–Pb dating of apatite by LA-ICPMS. Chem. Geol. 280, 200–216. https://doi.org/10.1016/j. chemgeo.2010.11.010.
- Chew, D.M., Petrus, J.A., Kamber, B.S., 2014a. U–Pb LA–ICPMS dating using accessory mineral standards with variable common Pb. Chem. Geol. 363, 185–199. https:// doi.org/10.1016/j.chemgeo.2013.11.006.
- Chew, D.M., Donelick, R.A., Donelick, M.B., Kamber, B.S., Stock, M.J., 2014b. Apatite chlorine concentration measurements by LA-ICP-MS. Geostand. Geoanal. Res. 38, 23–35. https://doi.org/10.1111/j.1751-908X.2013.00246.x.
- Chew, D.M., Babechuk, M.G., Cogné, N., Mark, C., O'Sullivan, G.J., Henrichs, I.A., Doepke, D., McKenna, C.A., 2016. (LA,Q)-ICPMS trace-element analyses of Durango and McClure Mountain apatite and implications for making natural LA-ICPMS mineral standards. Chem. Geol. 435, 35–48. https://doi.org/10.1016/j. chemgeo.2016.03.028.
- Chew, D.M., Petrus, J.A., Kenny, G.G., McEvoy, N., 2017. Rapid high-resolution U–Pb LA-Q-ICPMS age mapping of zircon. J. Anal. At. Spectrom. 32, 262–276. https://doi.org/10.1039/C61A00404K
- Cochrane, R., Spikings, R.A., Chew, D., Wotzlaw, J.-F., Chiaradia, M., Tyrrell, S., Schaltegger, U., Van der Lelij, R., 2014. High temperature (>350°C) thermochronology and mechanisms of Pb loss in apatite. Geochim. Cosmochim. Acta 127, 39–56. https://doi.org/10.1016/j.gca.2013.11.028.
- Condon, D.J., Schoene, B., McLean, N.M., Bowring, S.A., Parrish, R.R., 2015. Metrology and traceability of U-Pb isotope dilution geochronology (EARTHTIME Tracer Calibration Part I). Geochim. Cosmochim. Acta 164, 464–480. https://doi.org/ 10.1016/j.gca.2015.05.026.
- Coulson, I.M., Villeneuve, M.E., Dipple, G.M., Duncan, R.A., Russell, J.K., Mortensen, J. K., 2002. Time-scales of assembly and thermal history of a composite felsic pluton: Constraints from the Emerald Lake area, northern Canadian Cordillera, Yukon. J. Volcanol. Geotherm. Res. 114, 331–356. https://doi.org/10.1016/S0377-0273 (01)00294-3.
- Dubois, J.C., Retali, G., Cesario, J., 1992. Isotopic analysis of rare earth elements by total vaporization of samples in thermal ionization mass spectrometry. Int. J. Mass Spectrom. Ion Process. 120, 163–177. https://doi.org/10.1016/0168-1176(92) 85046-3.
- Elburg, M., Vroon, P., van der Wagt, B., Tchalikian, A., 2005. Sr and Pb isotopic composition of five USGS glasses (BHVO-2G, BIR-1G, BCR-2G, TB-1G, NKT-1G). Chem. Geol. 223, 196–207. https://doi.org/10.1016/j.chemgeo.2005.07.001.
- Emo, R.B., Smit, M.A., Schmitt, M., Kooijman, E., Scherer, E.E., Sprung, P., Bleeker, W., Mezger, K., 2018. Evidence for evolved Hadean crust from Sr isotopes in apatite within Eoarchean zircon from the Acasta Gneiss complex. Geochim. Cosmochim. Acta 235, 450–462. https://doi.org/10.1016/j.gca.2018.05.028.
- Fisher, C.M., McFarlane, C.R.M., Hanchar, J.M., Schmitz, M.D., Sylvester, P.J., Lam, R., Longerich, H.P., 2011. Sm–Nd isotope systematics by laser ablation-multicollectorinductively coupled plasma mass spectrometry: Methods and potential natural and synthetic reference materials. Chem. Geol. 284, 1–20. https://doi.org/10.1016/j. chemgeo.2011.01.012.
- Fisher, C.M., Bauer, A.M., Luo, Y., Sarkar, C., Hanchar, J.M., Vervoort, J.D., Tapster, S.R., Horstwood, M., Pearson, D.G., 2020a. Laser ablation split-stream analysis of the SmNd and U-Pb isotope compositions of monazite, titanite, and apatite Improvements, potential reference materials, and application to the Archean Saglek Block gneisses. Chem. Geol. 539, 119493 https://doi.org/10.1016/j.chemgeo.2020.119493.
- Fisher, C.M., Bauer, A.M., Vervoort, J.D., 2020b. Disturbances in the Sm-Nd isotope system of the Acasta Gneiss Complex—Implications for the Nd isotope record of the early Earth. Earth Planet. Sci. Lett. 530, 115900 https://doi.org/10.1016/j. epsl.2019.115900.
- Gillespie, J., Nemchin, A.A., Kinny, P.D., Martin, L., Aleshin, M., Roberts, M.P., Ireland, T.R., Whitehouse, M.J., Jeon, H., Cavosie, A.J., Kirkland, C.L., 2021a. Strontium isotope analysis of apatite via SIMS. Chem. Geol. 559, 119979 https://doi. org/10.1016/j.chemgeo.2020.119979.
- Gehrels, G.E., Valencia, V.A., Ruiz, J., 2008. Enhanced precision, accuracy, efficiency, and spatial resolution of U-Pb ages by laser ablation-multicollector-inductively coupled plasma-mass spectrometry. Geochem. Geophys. Geosyst. 9 https://doi.org/10.1029/2007GC001805.
- Gerstenberger, H., Haase, G., 1997. A highly effective emitter substance for mass spectrometric Pb isotope ratio determinations. Chem. Geol. 136, 309–312. https:// doi.org/10.1016/S0009-2541(96)00033-2.
- Gillespie, J., Kinny, P.D., Kirkland, C.L., Martin, L., Nemchin, A.A., Cavosie, A.J., Hasterok, D., 2021b. Isotopic modelling of Archean crustal evolution from

- comagmatic zircon–apatite pairs. Earth Planet. Sci. Lett. 575, 117194 https://doi.org/10.1016/j.epsl.2021.117194.
- Glorie, S., Jepson, G., Konopelko, D., Mirkamalov, R., Meeuws, F., Gilbert, S., Gillespie, J., Collins, A.S., Xiao, W., Dewaele, S., De Grave, J., 2019. Thermochronological and geochemical footprints of post-orogenic fluid alteration recorded in apatite: Implications for mineralisation in the Uzbek Tian Shan. Gondwana Res. 71, 1–15. https://doi.org/10.1016/j.gr.2019.01.011.
- Hammerli, J., Kemp, A.I.S., Whitehouse, M.J., 2019. In situ trace element and Sm-Nd isotope analysis of accessory minerals in an Eoarchean tonalitic gneiss from Greenland: Implications for Hf and Nd isotope decoupling in Earth's ancient rocks. Chem. Geol. 524, 394–405. https://doi.org/10.1016/j.chemgeo.2019.06.025.
- Harlov, D.E., Wirth, R., Förster, H.-J., 2005. An experimental study of dissolution-reprecipitation in fluorapatite: fluid infiltration and the formation of monazite. Contrib. Mineral. Petrol. 150, 268–286. https://doi.org/10.1007/s00410-005-0017-8.
- Henderson, A.L., Foster, G.L., Najman, Y., 2010. Testing the application of in situ Sm-Nd isotopic analysis on detrital apatites: A provenance tool for constraining the timing of India-Eurasia collision. Earth Planet. Sci. Lett. 297, 42–49. https://doi.org/10.1016/i.epsl.2010.06.001.
- Henrichs, I.A., O'Sullivan, G., Chew, D.M., Mark, C., Babechuk, M.G., McKenna, C., Emo, R., 2018. The trace element and U-Pb systematics of metamorphic apatite. Chem. Geol. 483, 218–238. https://doi.org/10.1016/j.chemgeo.2017.12.031.
- Horn, I., Rudnick, R.L., McDonough, W.F., 2000. Precise elemental and isotope ratio determination by simultaneous solution nebulization and laser ablation-ICP-MS: application to U-Pb geochronology. Chem. Geol. 164, 281–301. https://doi.org/ 10.1016/S0009-2541(99)00168-0.
- Horstwood, M.S.A., Evans, J.A., Montgomery, J., 2008. Determination of Sr isotopes in calcium phosphates using laser ablation inductively coupled plasma mass spectrometry and their application to archaeological tooth enamel. Geochim. Cosmochim. Acta 72, 5659–5674. https://doi.org/10.1016/j.gca.2008.08.016.
- Horstwood, M.S.A., Košler, J., Gehrels, G., Jackson, S.E., McLean, N.M., Paton, C., Pearson, N.J., Sircombe, K., Sylvester, P., Vermeesch, P., Bowring, J.F., Condon, D.J., Schoene, B., 2016. Community-derived standards for LA-ICP-MS U-(Th-)Pb geochronology – uncertainty propagation, age interpretation and data reporting. Geostand. Geoanal. Res. 40, 311–332. https://doi.org/10.1111/j.1751-908X.2016.00379.x.
- Hou, K.J., Qin, Y., Li, Y.H., Fan, C.F., 2013. In situ Sr, Nd isotopic measurement of apatite using laser ablation multi-collector inductively coupled plasma mass spectrometry. Rock Miner. Anal. 32 (8), 547–554 (in Chinese with English abstract).
- Ibanez-Mejia, M., Bloch, E.M., Vervoort, J.D., 2018. Timescales of collisional metamorphism from Sm-Nd, Lu-Hf and U-Pb thermochronology: a case from the Proterozoic Putumayo Orogen of Amazonia. Geochim. Cosmochim. Acta 235, 103–126. https://doi.org/10.1016/j.gca.2018.05.017.
  Isnard, H., Brennetot, R., Caussignac, C., Caussignac, N., Chartier, F., 2005.
- Isnard, H., Brennetot, R., Caussignac, C., Caussignac, N., Chartier, F., 2005. Investigations for determination of Gd and Sm isotopic compositions in spent nuclear fuels samples by MC ICPMS. Int. J. Mass Spectrom. 246, 66–73. https://doi.org/ 10.1016/j.ijms.2005.08.008.
- Jaffey, A.H., Flynn, K.F., Glendenin, L.E., Bentley, W.C., Essling, A.M., 1971. Precision measurement of half-lives and specific activities of 235U and 238U. Phys. Rev. C 4, 1889–1906. https://doi.org/10.1103/PhysRevC.4.1889.
- Jochum, K.P., Weis, U., Stoll, B., Kuzmin, D., Yang, Q., Raczek, I., Jacob, D.E., Stracke, A., Birbaum, K., Frick, D.A., Günther, D., Enzweiler, J., 2011. Determination of reference values for NIST SRM 610-617 glasses following ISO guidelines. Geostand. Geoanal. Res. 35, 397–429. https://doi.org/10.1111/j.1751-908X 2011.00120 x
- Kent, A.J.R., Ungerer, C.A. Andy, 2005. Production of barium and light rare earth element oxides during LA-ICP-MS microanalysis. J. Anal. At. Spectrom. 20, 1256. https://doi.org/10.1039/b505734e.
- Kirkland, C.L., Yakymchuk, C., Szilas, K., Evans, N., Hollis, J., McDonald, B., Gardiner, N. J., 2018. Apatite: a U-Pb thermochronometer or geochronometer? Lithos 318–319, 143–157. https://doi.org/10.1016/j.lithos.2018.08.007.
- Krestianinov, E., Amelin, Y., Neymark, L.A., Aleinikoff, J.N., 2021. U-Pb systematics of uranium-rich apatite from Adirondacks: Inferences about regional geological and geochemical evolution, and evaluation of apatite reference materials for in situ dating. Chem. Geol. 581, 120417 https://doi.org/10.1016/j.chemgeo.2021.120417.
- Krogh, T.E., 1973. A low-contamination method for hydrothermal decomposition of zircon and extraction of U and Pb for isotopic age determinations. Geochim. Cosmochim. Acta 87, 485–494.
- Krogstad, E.J., Walker, R.J., 1994. High closure temperatures of the U-Pb system in large apatites from the Tin Mountain pegmatite, Black Hills, South Dakota, USA. Geochim. Cosmochim. Acta 58, 3845–3853. https://doi.org/10.1016/0016-7037(94)90367-0.
- Kylander-Clark, A.R.C., 2017. Petrochronology by laser-ablation inductively coupled plasma nass spectrometry. Rev. Miner. Geochem. 83, 183–198. https://doi.org/ 10.2138/rmg.2017.83.6.
- Kylander-Clark, A.R.C., Hacker, B.R., Cottle, J.M., 2013. Laser-ablation split-stream ICP petrochronology. Chem. Geol. 345, 99–112. https://doi.org/10.1016/j.chemgeo.2013.02.019.
- Ludwig, K.R., 2012. User's Manual for Isoplot 3.75, A Geochronological Toolkit for Microsoft Excel, Berkeley Geochronology Center Special Publication No. 5.
- Mao, M., Rukhlov, A.S., Rowins, S.M., Spence, J., Coogan, L.A., 2016. Apatite trace element compositions: a robust new tool for mineral exploration. Econ. Geol. 111, 1187–1222. https://doi.org/10.2113/econgeo.111.5.1187.
- McCubbin, F.M., Jones, R.H., 2015. Extraterrestrial apatite: planetary geochemistry to astrobiology. Elements 11, 183–188. https://doi.org/10.2113/gselements.11.3.183.

Chemical Geology 590 (2022) 120689

- McDowell, F.W., McIntosh, W.C., Farley, K.A., 2005. A precise 40Ar–39Ar reference age for the Durango apatite (U–Th)/He and fission-track dating standard. Chem. Geol. 214, 249–263. https://doi.org/10.1016/j.chemgeo.2004.10.002.
- McFarlane, C.R.M., McCulloch, M.T., 2007. Coupling of in-situ Sm-Nd systematics and U-Pb dating of monazite and allanite with applications to crustal evolution studies. Chem. Geol. 245, 45-60. https://doi.org/10.1016/j.chemgeo.2007.07.020.
- McFarlane, C.R.M., McCulloch, M.T., 2008. Sm-Nd and Sr isotope systematics in LREE-rich accessory minerals using LA-MC-ICP-MS. In: Sylvester, P. (Ed.), Laser-Ablation ICPMS in the Earth Sciences: Current Practices and Outstanding Issues, 40. Mineralogical Association of Canada Short Course, pp. 117–133.
- McLean, N.M., Condon, D.J., Schoene, B., Bowring, S.A., 2015. Evaluating uncertainties in the calibration of isotopic reference materials and multi-element isotopic tracers (EARTHTIME Tracer Calibration Part II). Geochim. Cosmochim. Acta 164, 481–501. https://doi.org/10.1016/j.gca.2015.02.040.
- Morton, A., Yaxley, G., 2007. Detrital apatite geochemistry and its application in provenance studies. In: Sedimentary Provenance and Petrogenesis: Perspectives from Petrography and Geochemistry. Geological Society of America, pp. 319–344. https://doi.org/10.1130/2006.2420(19).
- O'Sullivan, G.J., Chew, D.M., 2020. The clastic record of a Wilson Cycle: evidence from detrital apatite petrochronology of the Grampian-Taconic fore-arc. Earth Planet. Sci. Lett. 552, 116588 https://doi.org/10.1016/j.epsl.2020.116588.
- O'Sullivan, G.J., Chew, D.M., Morton, A.C., Mark, C., Henrichs, I.A., 2018. An integrated apatite geochronology and geochemistry tool for sedimentary provenance analysis. Geochem. Geophys. Geosyst. 19, 1309–1326. https://doi.org/10.1002/2017GC007343.
- O'Sullivan, G., Chew, D., Kenny, G., Henrichs, I., Mulligan, D., 2020. The trace element composition of apatite and its application to detrital provenance studies. Earth-Sci. Rev. 201, 103044 https://doi.org/10.1016/j.earscirev.2019.103044.
- Paton, C., Hellstrom, J., Paul, B., Woodhead, J., Hergt, J., 2011. Iolite: Freeware for the visualisation and processing of mass spectrometric data. J. Anal. At. Spectrom. 26, 2508. https://doi.org/10.1039/c1ja10172b.
- Paul, A.N., Spikings, R.A., Chew, D., Daly, J.S., 2019. The effect of intra-crystal uranium zonation on apatite U-Pb thermochronology: a combined ID-TIMS and LA-MC-ICP-MS study. Geochim. Cosmochim. Acta 251, 15–35. https://doi.org/10.1016/j. gca.2019.02.013.
- Paul, A.N., Spikings, R.A., Gaynor, S.P., 2021. U-Pb ID-TIMS reference ages and initial Pb isotope compositions for Durango and Wilberforce apatites. Chem. Geol. 586, 120604 https://doi.org/10.1016/j.chemgeo.2021.120604.
- Pearce, N.J.G., Perkins, W.T., Westgate, J.A., Gorton, M.P., Jackson, S.E., Neal, C.R., Chenery, S.P., 1997. A compilation of new and published major and trace element data for NIST SRM 610 and NIST SRM 612 Glass reference materials. Geostand. Geoanal. Res. 21, 115–144. https://doi.org/10.1111/j.1751-908X.1997.tb00538.x.
- Petrus, J.A., Kamber, B.S., 2012. VizualAge: a novel approach to laser ablation ICP-MS U-Pb geochronology data reduction. Geostand. Geoanal. Res. 36, 247–270. https://doi.org/10.1111/j.1751-908X.2012.00158.x.
- Piccoli, P.M., Candela, P.A., 2002. Apatite in igneous systems. Rev. Mineral. Geochem. 48, 255–292. https://doi.org/10.2138/rmg.2002.48.6.
- Poletti, J.E., Cottle, J.M., Hagen-Peter, G.A., Lackey, J.S., 2016. Petrochronological constraints on the origin of the Mountain Pass ultrapotassic and carbonatite Intrusive Suite, California. J. Petrol. 57, egw050. https://doi.org/10.1093/petrology/egw050.
- Prowatke, S., Klemme, S., 2006. Trace element partitioning between apatite and silicate melts. Geochim. Cosmochim. Acta 70, 4513–4527. https://doi.org/10.1016/j. gca.2006.06.162.

- Ramos, F.C., Wolff, J.A., Tollstrup, D.L., 2004. Measuring 87Sr/86Sr variations in minerals and groundmass from basalts using LA-MC-ICPMS. Chem. Geol. 211, 135–158. https://doi.org/10.1016/j.chemgeo.2004.06.025.
- Ravindran, A., Mezger, K., Balakrishnan, S., Kooijman, E., Schmitt, M., Berndt, J., 2020. Initial 87Sr/86Sr as a sensitive tracer of Archaean crust-mantle evolution: Constraints from igneous and sedimentary rocks in the western Dharwar Craton, India. Precambrian Res. 337, 105523 https://doi.org/10.1016/j. precamres.2019.105523.
- Sano, Y., Oyama, T., Terada, K., Hidaka, H., 1999. Ion microprobe U-Pb dating of apatite. Chem. Geol. 153, 249–258. https://doi.org/10.1016/S0009-2541(98) 00163-6.
- Schmitz, M.D., Schoene, B., 2007. Derivation of isotope ratios, errors, and error correlations for U-Pb geochronology using 205 Pb- 235 U-( 233 U)-spiked isotope dilution thermal ionization mass spectrometric data. Geochem. Geophys. Geosyst. 8 https://doi.org/10.1029/2006GC001492 n/a-n/a.
- Schoene, B., Bowring, S.A., 2006. U-Pb systematics of the McClure Mountain syenite: thermochronological constraints on the age of the 40Ar/39Ar standard MMhb. Contrib. Mineral. Petrol. 151, 615–630. https://doi.org/10.1007/s00410-006-0077-4.
- Schoene, B., Bowring, S.A., 2007. Determining accurate temperature–time paths from U–Pb thermochronology: An example from the Kaapvaal craton, southern Africa. Geochim. Cosmochim. Acta 71, 165–185. https://doi.org/10.1016/j. gca.2006.08.029.
- Seymour, N.M., Stockli, D.F., Beltrando, M., Smye, A.J., 2016. Tracing the thermal evolution of the Corsican lower crust during Tethyan rifting. Tectonics 35, 2439–2466. https://doi.org/10.1002/2016TC004178.
- Spear, F.S., Pyle, J.M., 2002. Apatite, monazite, and xenotime in metamorphic rocks. Rev. Mineral. Geochem. 48, 293–335. https://doi.org/10.2138/rmg.2002.48.7.
- Stacey, J.S., Kramers, J.D., 1975. Approximation of terrestrial lead isotope evolution by a two-stage model. Earth Planet. Sci. Lett. 26, 207–221. https://doi.org/10.1016/ 0012-821X/75190088-6
- Sylvester, P.J., 2008. LA-(MC)-ICP-MS trends in 2006 and 2007 with particular emphasis on measurement uncertainties. Geostand. Geoanalyt. Res. 32, 469–488. https://doi. org/10.1111/j.1751-908X.2008.00924.x.
- Thompson, J., Meffre, S., Maas, R., Kamenetsky, V., Kamenetsky, M., Goemann, K., Ehrig, K., Danyushevsky, L., 2016. Matrix effects in Pb/U measurements during LA-ICP-MS analysis of the mineral apatite. J. Anal. At. Spectrom. 31, 1206–1215. https://doi.org/10.1039/C6JA00048G.
- Thomson, S.N., Gehrels, G.E., Ruiz, J., Buchwaldt, R., 2012. Routine low-damage apatite U-Pb dating using laser ablation-multicollector-ICPMS. Geochem. Geophys. Geosyst. 13 https://doi.org/10.1029/2011GC003928 n/a-n/a.
- Vance, D., Thirlwall, M., 2002. An assessment of mass discrimination in MC-ICPMS using Nd isotopes. Chem. Geol. 185, 227–240. https://doi.org/10.1016/S0009-2541(01) 00402-8.
- Vermeesch, P., 2018. IsoplotR: a free and open toolbox for geochronology. Geosci. Front. 9, 1479–1493. https://doi.org/10.1016/j.gsf.2018.04.001.
- Wendt, I., Carl, C., 1991. The statistical distribution of the mean squared weighted deviation. Chem. Geol. Isot. Geosci. Sect. 86, 275–285. https://doi.org/10.1016/ 0168-9622(91)90010-T.
- Yang, Y.H., Wu, F.Y., Yang, J.H., Chew, D.M., Xie, L.W., Chu, Z.Y., Zhang, Y. Bin, Huang, C., 2014. Sr and Nd isotopic compositions of apatite reference materials used in U-Th-Pb geochronology. Chem. Geol. 385, 35–55. https://doi.org/10.1016/j. chemseo.2014.07.012.